

TOPICAL REVIEW

## Current trends in planar Hall effect sensors: evolution, optimization, and applications

To cite this article: Amir Elzawwy *et al* 2021 *J. Phys. D: Appl. Phys.* **54** 353002

View the [article online](#) for updates and enhancements.

### You may also like

- [Revealing the origin of the vertical hysteresis loop shifts in an exchange biased Co/YMnO<sub>2</sub> bilayer](#)  
J Barzola-Quiquia, A Lessig, A Ballestar *et al.*
- [Finite transverse conductance and anisotropic magnetoconductance under an applied in-plane magnetic field in two-dimensional electron gases with strong spin-orbit coupling](#)  
Abhiram Soori
- [Manipulating the magnetic and transport properties by Culr thickness in CoFeB/Culr/IrMn multilayers](#)  
Mustafa Öztürk and Erdem Demirci



**ECS**  
The  
Electrochemical  
Society  
Advancing solid state &  
electrochemical science & technology

**DISCOVER**  
how sustainability  
intersects with  
electrochemistry & solid  
state science research

## Topical Review

# Current trends in planar Hall effect sensors: evolution, optimization, and applications

Amir Elzawy<sup>1,\*</sup> , Hasan Pişkin<sup>2</sup> , Numan Akdoğan<sup>3</sup> , Marius Volmer<sup>4</sup> ,  
Günter Reiss<sup>5</sup> , Luca Marnitz<sup>5</sup>, Anastasiia Moskaltsova<sup>5</sup>, Ogan Gurel<sup>6,7</sup>  
and Jan-Michael Schmalhorst<sup>5</sup>

<sup>1</sup> Ceramics Department, Inorganic Chemistry Industries and Mineral Resources Division, National Research Centre, El-Bohouth Str., Cairo 12622, Egypt

<sup>2</sup> Department of Physics, Boğaziçi University, Istanbul, 34342, Turkey

<sup>3</sup> Department of Physics, Gebze Technical University, Gebze, Kocaeli 41400, Turkey

<sup>4</sup> Electrical Engineering and Applied Physics Department, Transilvania University of Brasov, Brasov 500036, Romania

<sup>5</sup> Thin Films & Physics of Nanostructures, Center for Spinelectronic Materials and Devices, Department of Physics, Bielefeld University, Bielefeld 33615, Germany

<sup>6</sup> College of Transdisciplinary Studies, DGIST, Daegu 42988, Republic of Korea

<sup>7</sup> Flite Material Sciences, Montreal, Canada

E-mail: [elzawy1@gmail.com](mailto:elzawy1@gmail.com) and [aa.elzawy@nrc.sci.eg](mailto:aa.elzawy@nrc.sci.eg)

Received 18 February 2021, revised 15 April 2021

Accepted for publication 27 April 2021

Published 30 June 2021



## Abstract

The advantages of planar Hall effect (PHE) sensors—their thermal stability, very low detection limits, and high sensitivities—have supported a wide range of advanced applications such as nano-Tesla (nT) magnetometers, current sensing, or low magnetic moment detection in lab-on-a-chip devices. In this review we outline the background and implications of these PHE sensors, starting from fundamental physics through their technological evolution over the past few decades. Key parameters affecting the performance of these sensors, including noise from different sources, thermal stability, and magnetoresistance magnitudes are discussed. The progression of sensor geometries and junctions from disk, cross-to-bridge, ring, and ellipse configuration is also reviewed. The logical sequence of these structures from single magnetoresistive layers to bi-, tri-layers, and spin-valves is also covered. Research contributions to the development of these sensors are highlighted with a focus on microfluidics and flexible sensorics. This review serves as a comprehensive resource for scientists who wish to use PHE for fundamental research or to develop new applications and devices. The conclusions from this report will benefit the development, production, and performance evaluation of PHE-based devices and microfluidics, as well as set the stage for future advances.

Keywords: planar Hall effect, sensors, permalloy, magnetoresistance, thin films, NiFe/IrMn

(Some figures may appear in colour only in the online journal)

\* Author to whom any correspondence should be addressed.

## 1. Introduction

Technologies that improve life are always in increasing demand. Spintronics—also known as spin electronics—which combines the charge and spin characteristics of electrons, offers a variety of novel and powerful device possibilities to provide such solutions. These devices find use in several key applications such as magnetometers, magnetic compasses, magnetic memories, or as sensing elements in conjunction with lab-on-a-chip (LOC) devices and point-of-care systems. Different types of sensors may be employed in these devices, as with electrochemical sensors [1–9], pressure sensors [10–13], temperature sensors [14, 15], gas sensors [16, 17], and humidity sensors [18–20]. These familiar classes of sensors directly detect changes in the surrounding environment, whereas magnetic sensors do not directly measure such properties. Instead, these magnetic sensors measure disturbances in the applied magnetic field which can be converted into an electrical output voltage [21–23]. Basically, the information attained from the magnetic sensors (variations and fluctuations of the field) can be exploited to track the directions, locations, angles and rotations of items, the existence of an electric current, in nondestructive testing, and so on [24]. The working principle, then, for magnetic sensors does not involve direct, physical contact. This property, along with the fact that magnetic sensing has reduced noise in biological media, positions magnetic sensors ideally in the area of biodection [25–27]. In this review we focus on magnetic sensors based on ferromagnetic (FM) materials, not semiconducting material-based sensors. The key advantages for these sensors are improved response time, field linearity, reliability, reproducibility, sensitivity, selectivity, stability, ease of fabrication, and lower detection limits [28–37].

The market for magnetic field sensors is growing rapidly, estimated at ~\$20B (USD) in 2019 [38, 39]. Various physical phenomena are employed to develop magnetic field sensors, which include search-coil, micro (fluxgate) sensors [40], magnetoresistive, and Hall effect sensors, as based on galvanomagnetic effects in semiconductors and magnetic thin films [41]. Despite their high sensitivity, search-coil and fluxgate magnetometers require complex electronic circuitry to deliver a useful voltage and are not compatible with integrated circuit (IC) technology, which, in turn, allows miniaturization, portability, and low power consumption. On the other hand, magnetoresistance (MR) and Hall effect sensors offer many benefits because they both compatible with and readily interfaced with IC technology, and thus can be integrated on the same chip in both analog and digital electronic circuits. With respect to sensor performance, their application areas are well established and distinct. MR sensors made from magnetic layers are considered to be highly sensitive and ideal for small magnetic fields between  $10^{-9}$  T to  $10^{-2}$  T, whereas Hall sensors, constructed from semiconductors, are less sensitive and more optimal for magnetic fields greater than  $10^{-6}$  T [42]. In contrast, however, with MR sensors, semiconductor-based Hall sensors show no saturation effects at high magnetic fields. It should be noted that, for MR-based sensors, these limits are strongly influenced by the magnetic properties of the materials

and the layout of the microfabricated sensors. There is an increasing number of applications that require magnetic field sensors with improved performances like high sensitivity, low hysteretic behavior, low noise, and low thermal drift. Also, some special applications require magnetic sensors with tunable properties to fine adapt their field characteristics to the specific use. The planar Hall sensors based on magnetoresistance has diverse applications. These include biosensing [43], flux leakage inspection [44], current sensing [45], and others [46]. Furthermore, from the field of wearable sensors for remote health monitoring, which has developed significantly in recent years, has given rise to many studies on the magnetic and electrical properties of structures deposited over flexible substrates [47–52].

The evolution of the number of publications and their total citations within 2002–2020 for the keyword, planar Hall effect (PHE) is screened in figure 1 based on the Web of Science core collection. However, in many other research papers, the PHE is used both as a tool for fundamental research or for sensing applications, so, the total number of published papers and citations regarding with this subject can be much higher.

In this review, we review the fundamentals of PHE sensors with respect to their origin, evolution, and configuration. From this, we proceed to FM and FM/antiferromagnetic (FM/AF) exchange-biased multilayer structures, discussing the optimizations performed for key parameters such as junction configuration, thermal stability, and signal-to-noise ratio (S/N). Finally, we highlight the major areas of application such as bio-detection, low magnetic moment sensing, and inspection of flux leakage for pipelines. We then offer perspectives on the future outlook and directions for the field.

In what follows we give a brief description of the most important MR effects that are used for fundamental research, i.e. investigation of magnetization processes and other related phenomena in nanostructured thin films, and to build magnetic sensors for applications such as high sensitivity magnetometers [47, 53], rotation encoders and micro compasses [54–58], current sensors [45, 59, 60], and magnetic nanoparticles (MNPs) detection for biosensing [61–64] in LOC devices.

## 2. Fundamentals of MR effects

The MR effect refers to a change in the electrical resistivity of a material depending on the externally applied magnetic field. For non-magnetic materials, the MR effect can be expressed by [29]:

$$\text{MR}(H)\% = \frac{R(H) - R(H=0)}{R(H=0)} \times 100\% \quad (1)$$

where  $R(H)$  and  $R(H=0)$  being the resistance of the material for an applied field,  $(H)$ , and  $H=0$ , respectively. In non-magnetic metals, for magnetic fields up to 1 T, the MR ratio is larger than 0 but is less than 1% and the effect is due to Lorentz forces that act on moving electrons.

For magnetic materials,  $H=0$  describes the remanent state which can depend on the magnetization history. For this

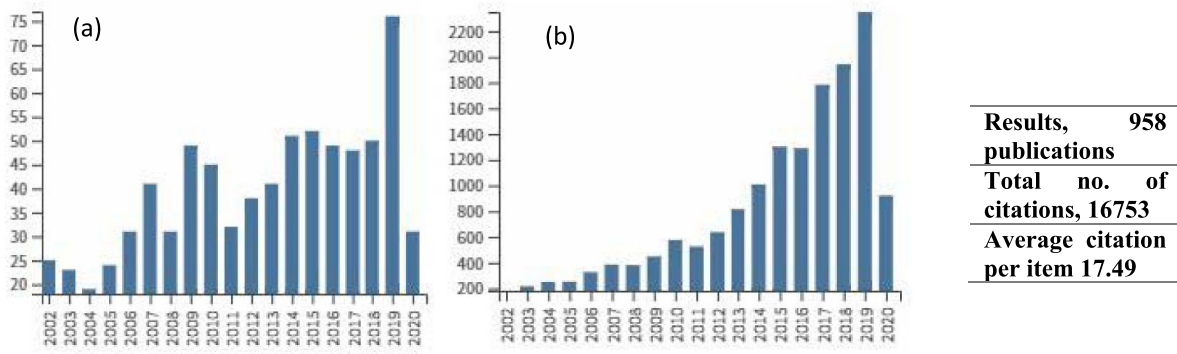


**Figure 1.** The evolution of number of papers dealing with planar Hall effect since 2002 according to Web of Science core collection (accessed 6-5-2020) (a) number of publications using the keyword ‘planar Hall effect’, (b) the total number of citations within the same years range.

reason, a more reliable state to describe the reference resistance is at saturation,  $H_{sat}$ , such that, for FM materials, a more appropriate description of the MR field dependence is [65, 66]:

$$MR(H) = \left( \frac{R(H) - R(H_{sat})}{R(H_{sat})} \right). \quad (2)$$

Note that the applications enumerated above are mostly based on Giant MR (GMR), Tunneling MR (TMR), Anisotropic MR effect (AMR), and PHE effects which will be briefly presented in what follows. Special attention will be paid to AMR and PHE.

### 2.1. GMR and TMR effects

The GMR effect was discovered in 1988 by Albert Fert [67], and Peter Grünberg [68] in exchange-coupled magnetic multilayered structures of the type  $(Fe/Cr)_n$ . Briefly, the resistance of a multilayer stack with an antiparallel magnetization configuration is larger in size as compared to that of a parallel magnetization configuration as shown in figure 2. The physical mechanism of the GMR effect is the spin-dependent scattering at the interfaces and in FM layers for spin-up (spin parallel to layer magnetization) and spin-down (spin antiparallel to layer magnetization) electrons [69, 70]. The exchange coupling between the FM layers (like Co, Fe, NiFe, etc) has an oscillatory behavior and for some specific values of the non-magnetic (NM) interlayer thickness is AF [71, 72]. Therefore, when aligning the magnetization directions of the FM layers from the initial antiparallel state, at zero field, to a parallel configuration by applying an external magnetic field, the electrical resistance of the layer stack decreases.

Figure 2(a) illustrates a simple GMR structure of the type FM1/NM/FM2 for  $H = -H_{sat}$  and  $H = 0$  and  $H = H_{sat}$  respectively for which the magnetic moments in both layers are parallel. The field behavior of the MR effect is quadratic, very similar to the AMR effect but the amplitude of the GMR effect is larger, up to 15% at room temperature. Figure 2(b)

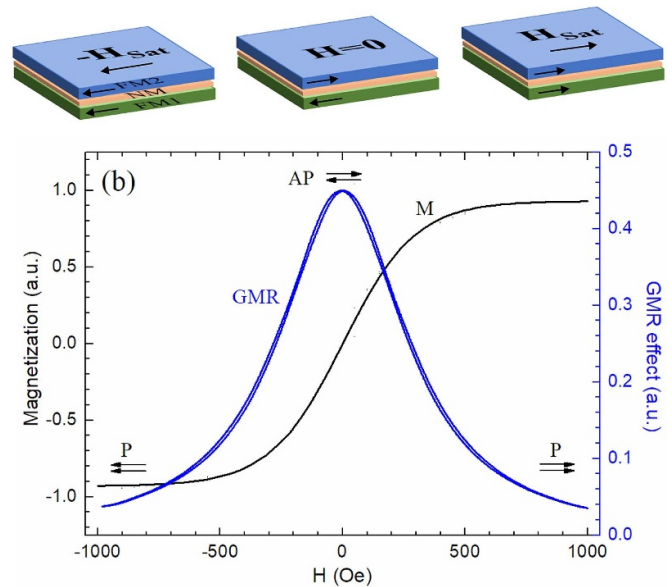


**Figure 2.** (a) Simple GMR 3-layer structure for three distinct states. i.e. for  $H = -H_{sat}$ ,  $H = 0$ , and  $H = H_{sat}$  respectively, and (b) typical field dependence of the structure magnetization and GMR by micromagnetic simulations.

shows the typical field behavior of the structure magnetization and the GMR effect obtained by micromagnetic simulations. Details regarding the parameters used for simulations are presented in [60].

A more convenient way to build a GMR sensor is to pin one of the FM layers with an adjacent AF layer through a unidirectional interface coupling effect named exchange bias [73, 74] while the other FM layer’s magnetization remains free to be switched by an externally applied magnetic field [39, 61, 75]. This is an exchange-biased spin-valve structure of the type FM/NM/FM/AF.

TMR is found in magnetic tunnel junctions (MTJs) with a structure very similar to that of spin valves where the conducting NM layer is replaced by a thin layer (around 1 nm) of insulating oxide like  $Al_2O_3$  or  $MgO$  [39, 76, 77]. The tunneling current through the insulating barrier of MTJs depends on

the relative orientation of the magnetizations of the FM layers, which gives rise to a TMR effect. The field dependence of the TMR effect is similar to that of the GMR effect but with a MR ratio up to 200% at room temperature [61, 77]. MTJ structures are used as magnetic sensors, spin tunnel read heads, and biomedical applications for detection of magnetic markers [78]. Now, MTJs are used as building blocks for magnetoresistive random access memories because of their small spatial footprint, which allows nanofabrication of high-density non-volatile memory cells [79].

Although TMR sensors can provide much larger signals when compared to GMR devices, the microfabrication processes of the TMR sensors are more complicated and expensive due to the need for ‘an upper contact.’ Therefore, a proper choice of device type is necessary for certain applications, as with, for example biosensing applications [77, 79]. For biosensing applications this means a larger distance between the magnetic nanoparticles (MNPs) and the free layer in the sensor which can lower the effective detection sensitivity of the field created by the MNPs. Moreover, the effective surface of the TMR sensors that can be exposed to MNPs is much lower than for GMR and PHE sensors and this affects the dynamic range in terms of the number of magnetic particles detected [80]. Finally, the resistance of TMR sensors is usually much larger as compared with GMR devices, and the corresponding noise is increased subsequently. For the detection of very low magnetic moments, elimination of noise requires an extended measuring period.

## 2.2. AMR and PHE effects

The AMR effect was discovered by William Thomson (Lord Kelvin) in 1856 and appears in FM bulk materials or thin films such as Ni, Co, Fe and their alloys [81, 82]. The AMR effect comes from the dependence of the electrical resistivity (hence the resistance as a measurable value) of a material on the angle between the direction of electric current and the direction of magnetization inside the material. In short, the physical origin of AMR can be attributed to the anisotropic s–d scattering of electrons due to the spin–orbit coupling on 3d orbitals of FM materials [56, 61, 83–85]. The net effect (in most magnetic materials) is that the electrical resistance has a maximum value when the direction of current is parallel to the magnetization and it has a minimum value when the direction of the current is perpendicular to the magnetization.

Thus, the AMR ratio that can be achieved in a magnetic material is expressed by [64, 86]

$$\frac{\Delta\rho}{\rho_{\perp}} = \left( \frac{\rho_{\parallel} - \rho_{\perp}}{\rho_{\perp}} \right) \times 100\% \quad (3)$$

where both resistivities  $\rho_{\parallel}$  and  $\rho_{\perp}$  are expressed at saturation field, parallel and perpendicular to the current direction respectively.

AMR devices, as single resistors, are more susceptible to thermal noise and thermal drift around zero fields [57]. However, as we can see from figure 3(a), when  $M$  rotates around  $\pm 45^{\circ}$  with the current direction, the AMR effect has linear variation. This has inspired the barber pole (BP) biasing where

the current is forced to flow in a direction that makes an angle of  $\pm 45^{\circ}$  with  $M$  [58]. Now, when  $H$  is applied over  $y$ -axis, the AMR effect will show a linear field dependence. The thin film elements are usually connected in a Wheatstone bridge configuration in order to compensate temperature drift and to double the signal output. This means that the AMR elements on the opposite arms are biased in the same way (at  $45^{\circ}$  and  $-45^{\circ}$  respectively) creating, in this way, a differential sensor. Ideally, the bridge resistances have the same value forming diagonal pairs of identical elements that react oppositely to one another to an external magnetic field. We must remark that this setup is equivalent, from an electric point of view, with a PHE structure [87, 88]. Several suppliers offer a large variety of commercially available devices based on AMR effect [54, 59, 89] and sensitivities of about  $0.35 \text{ (mV/V) Oe}^{-1}$  have been reported for Wheatstone bridges with BP-biased AMR sensors [58].

For most bulk magnetic materials this ratio is not larger than 5% whereas for typical FM NiFe films, the AMR value is in the order of 2%–2.2% in fields of a few Oe [58]. A widely used material is the Ni<sub>80</sub>Fe<sub>20</sub> (Permalloy) the magnetostriction and magnetocrystalline anisotropy both pass through zero near this composition [90].

To quantify the AMR and PHE, we may consider the measurement configuration given in figure 3(a). Here a thin film of FM material is presented. For functional devices, an easy axis of magnetization is defined by an anisotropy field ( $H_K$ ) through the shape anisotropy ( $l > w$ ) and the intrinsic anisotropy field due to the crystalline structure of the magnetic layer and microfabrication process.

The PHE output voltage is delivered as [91, 92]:

$$V_{\text{PHE}} = I \frac{(\rho_{\parallel} - \rho_{\perp})}{t} \sin\theta \cos\theta \quad (4)$$

where  $t$  is the thickness of the FM layer, and  $I$  is the constant current applied along the  $x$ -axis of the FM layer.

It can be mentioned here that the magnetization rotation can be due to a rotating magnetic field or to a magnetic field, ( $H$ ), which is applied along  $y$ -axis. The equilibrium state of magnetization angle ( $\theta$ ) in the sensing layer, can be calculated by minimizing the system’s free energy density ( $E_M$ ) expressed by [93–96]

$$E_M = K_u \sin^2\theta - M_S H \cos(\alpha - \theta) - M_S H_{\text{ex}} \cos(\beta - \theta) \quad (5)$$

where  $K_u$  is the effective anisotropy constant,  $M_S$  is the saturation magnetization and  $H_{\text{ex}}$  is the exchange biasing field, which acts like an external biasing (unidirectional) field applied to the sensing layer.  $\alpha$  is the angle between the external field, ( $H$ ), and the easy axis (anisotropy axis).  $\beta$  is the angle between the direction of the exchange bias field and the easy axis of the magnetic layer. Usually, in PHE sensors  $\beta$  is adjusted as  $0^{\circ}$ . Thus, under the zero magnetic field ( $H = 0$ ), the magnetization can be aligned along the current direction (along  $+x$ -axis), figure 3(a). For this device configuration, because  $\theta = 0$ , theoretically, the  $V_{\text{PHE}}$  given in equation (4) provides

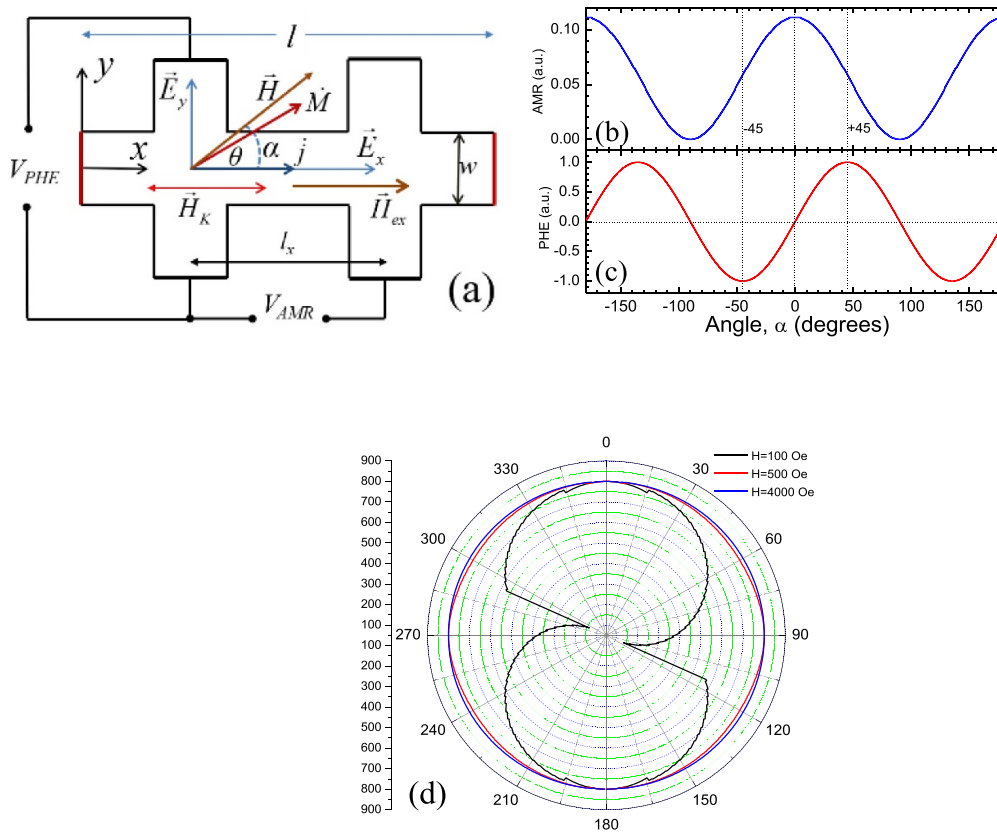


**Figure 3.** (a) Schematic representation of a Permalloy thin film through which is flowing a current along  $x$ -axis;  $M$  is the magnetization which makes an angle  $\theta$  with the current direction due to the applied field,  $H$ . A uniaxial magnetic anisotropy, defined by  $H_K$  may be present; (b), (c) the angular dependencies of the AMR and PHE respectively; (d) the angular dependence of magnetization along the rotating field  $H = 100, 500,$  and  $4000$  Oe.

zero voltage, therefore the PHE sensors are providing zero offset voltage. In addition, in many cases, the effect of the anisotropy can be described by an anisotropy field of ( $H_K$ ) rather by the anisotropy constant of ( $K_u$ ), (where  $H_K = 2K_u/M_S$ ) [97].

The position at the equilibrium of magnetization, and hence the angle  $\theta$ , is calculated from the energy minimum condition,  $dE_M/d\theta = 0$ , using a semi-analytical Stoner–Wohlfarth (SW) model implemented in SimulMag [55, 98].

Figures 3(b) and (c) show the dependencies of the AMR effect and PHE, respectively, on the angle  $\alpha$  between the rotating field  $H$  and  $j$ . These plots, which have a qualitative character, were obtained by considering a single domain of Permalloy ( $Ni_{80}Fe_{20}$ ), with  $l \times w \times t = 1000 \times 500 \times 10 \text{ nm}^3$  ( $t$  being the film thickness),  $M_S = 800 \text{ emu cm}^{-3}$  and  $H_K = 90 \text{ Oe}$ . A rotating field  $H = 4000 \text{ Oe}$  was employed in these simulations. The position at the equilibrium of magnetization, and hence the angle  $\theta$  between  $M$  and  $j$ , was obtained by minimizing the system’s free energy using a semi-analytical SW model implemented in SimulMag [55, 98]. Figure 3(d) shows that if  $H$  is large enough, i.e. larger than the effective anisotropy field,  $M$  follows accurately the field orientation, i.e.  $\alpha = \theta$ , and this suggests the application of AMR and PHE for rotation sensors.

As mentioned above, the magnetization can rotate, also, because of a field  $H$  applied over  $y$ -axis, i.e.  $\alpha = 90^\circ$  in

figure 3(a). This is the typical setup used for field sensing we present, in figure 4(a) and in figure 4(b) the field dependencies of the AMR effect and PHE simulated in the single domain approach. Now, comparing the results from figures 3 and 4 we can draw some conclusions: (a) the sensitivity of the AMR effect around zero-field (which can mean also,  $\theta = 0$ ) is very small and is 0 for  $H = 0$  whereas the response of the PHE is linear around zero-field, with a constant sensitivity; (b) the AMR signal is unipolar, with a quadratic field dependence, whereas the PHE signal is bipolar both for angular and field dependencies and (c) by applying a biasing field,  $H_{ex}$ , along the easy axis we can fine tune the AMR and PHE field response [56, 62]. The peak field- $H_p$  (for which  $\theta = 45^\circ$ ) expresses the maximum value of the applied field for which the sensor can deliver a useful signal, figure 4(b). This field can be expressed as [93]:

$$H_p = H_{ex} + H_K/\sqrt{2}. \tag{6}$$

With  $H_K$ , the effective anisotropy field which includes uniaxial anisotropy, the shape anisotropy, etc;  $H_{ex}$  is the exchange biasing field present in exchange biased and spin-valve structures or can be an external field,  $H_{ex}$ , applied along the current direction, figure 3(a) [62].

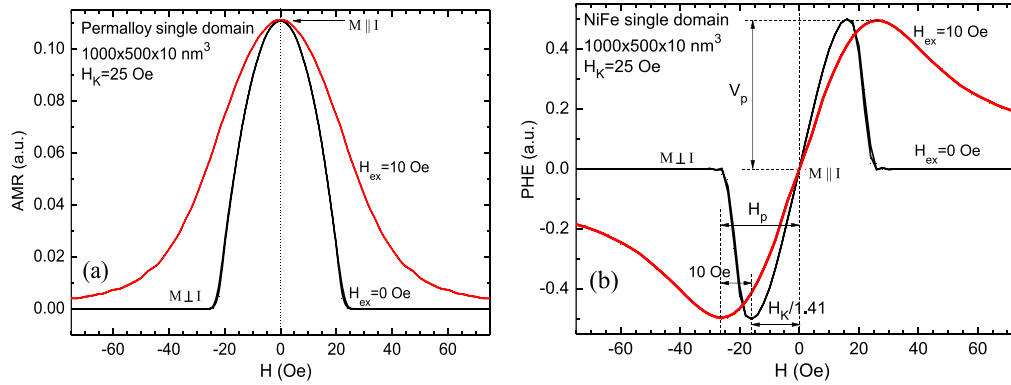


**Figure 4.** Field dependencies for (a) AMR effect and (b) PHE;  $H$  is directed along  $y$ -axis. The simulations were done, using the parameters presented above, for  $H_{ex} = 0$  and  $H_{ex} = 10$  Oe.

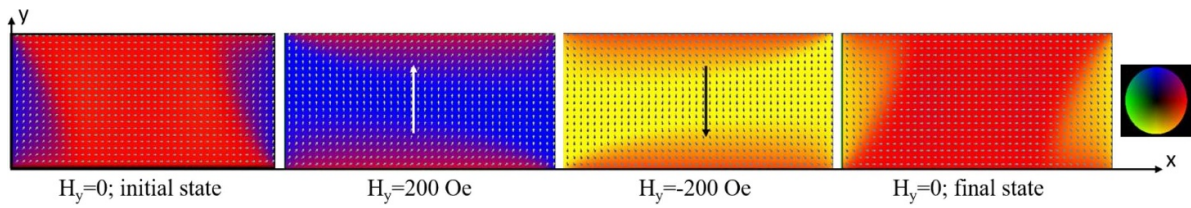


**Figure 5.** Illustration of magnetic moments orientation in a thin film of Permalloy  $1000 \times 500 \times 10 \text{ nm}^3$ . The used parameters are: cell dimension  $5 \text{ nm}$ ,  $M_S = 710 \text{ emu cm}^{-3}$ , exchange constant  $A = 1.3 \times 10^{-11} \text{ J m}^{-1}$ , and the anisotropy constant  $K_u = 500 \text{ J m}^{-3}$  along the  $x$ -axis;  $T_{abs} = 0 \text{ K}$ . The color legend illustrates the magnetic moments orientation.

These data show that PHE signals can be used to build low magnetic field sensors but can also be used as a sensitive tool to characterize magnetic thin films. As we will show later, PHE sensors are more sensitive to catch fluctuations in the direction of FM layer magnetization. Exactly controlling the magnetization state is key to the operation of PHE sensors. Ideally, the magnetization must be confined to a certain direction in zero field, and the application of a field perpendicular to this direction rotates the magnetization in such a way that the output signal,  $V_{PHE}$ , is linear with respect to the magnitude of the applied field. This is true for applied fields smaller than a fourth of the intrinsic effective anisotropy field, given for magnetocrystalline anisotropy, uniaxial anisotropy induced during the film deposition and the shape anisotropy. Magnetoelastic anisotropy becomes important when tension is present in the substrate. Such cases can be found when, for example, a piezoelectric material or a flexible material, like Kapton is used as substrate [47].

PHE sensors acquire the advantages of high linearity at small applied fields, elevated S/N ratio, reduced noise and zero-offset, as well as enhanced thermal stability and low power consumption [32, 64, 99–105]. Generally the sensitivity can be referred to as the ratio of the response to cause, hence the PHE sensitivity can be expressed as the ratio between the noticed output voltage and the operating field range, simply denoted as:  $S_{PHE} = \Delta V / \Delta H$  [97, 106].

From equation (6) and figure 4(b) it appears that higher sensitivities can be achieved for lower values of  $H_p$ . However, for real structures, smaller values for  $H_K$  and  $H_{ex}$  means magnetic domains in the sensing layer, figure 3, that imply

nonlinear field dependence and hysteretic behavior of the PHE signal [62]. On the other hand, larger values of  $H_{ex}$  and  $H_K$  bring the sensing layer close to a single domain structure with the cost of magnetic field sensitivity [93].

Finally, we must note that AMR and PHE dependencies may be affected by hysteretic effects in real structures, like NiFe films, which are far from single domain behavior, even if an easy axis of magnetization is defined through shape and uniaxial anisotropy. Figure 5 presents the results of micromagnetic simulations using LLG Micromagnetics simulator [107], performed on a Permalloy thin film of  $1000 \times 500 \times 10 \text{ nm}^3$  where the structure arrives in a final state which is slightly different from the initial state. This is translated into a different AMR or PHE signal at the sensor output.

Note that, the internal magnetization has no preferred direction along the longitudinal axis and flipping of  $180^\circ$  can occur due to spikes or to exposure to some external magnetic fields. This flipping of the magnetization results in a different sensitivity of the system. To overcome this problem an internal coil (KMZ51) or external controlled magnetic field should be used to reset and set the magnetization to the initial orientation. Other methods to keep the initial magnetization state, for  $H = 0$ , is to use exchange-biased structures like bilayers FM/AF, trilayers FM/NM/AF, or spin valves of the type FM/NM/FM/AF where FM is a FM layer (NiFe, NiFeCo, etc.), NM is a NM layer like Cu, Ag, Pt and AF is an AF layer like FeMn or IrMn [93]. These methods with their advantage and drawbacks will be discussed, later.

In this review article we focus on the use of NiFe as FM layer and IrMn as AF layer, as being representative for applications of PHE sensors. Other FM materials were studied with these bi- and tri-layer structures such as NiCo [108, 109], NiFeMo [100], CoFe [110], and others [91, 109, 111]. NiFe is a better candidate according to its MR value, diminished magnetostriction, and anisotropy, along with an easier domain rotation depending on excellent soft properties with reduced coercive field and increased saturation [112]. Previous studies were dedicated to using various AF materials as FeMn [113], NiMn [114, 115], NiO [116, 117], to exchange bias the NiFe layer. Presently, IrMn is the better choice to be used with NiFe, as it gives a higher exchange bias field, elevated thermal stability, and higher Néel temperature [118, 119].

### 2.3. A brief history of the PHE

Earlier studies of the PHE were reported more than five decades ago [120–124]. The term itself was first mentioned as a new galvanomagnetic effect by Goldberg, *et al* [121], where the authors introduced a new term ‘planar Hall field’, which is observed by measuring the induced voltage normal to the direction of current flow as in the conventional Hall effect configuration but with the magnetic field in the current–voltage plane. No earlier discussions or reports can be found regarding this topic. Sometimes this effect is cited as “pseudo Hall effect,” as the design of the experimental measurement mimics the conventional Hall effect excluding the field orientation [104, 115]. The study of theoretical basics of PHE was conducted by Ky [123, 124]. Additionally, PHE in a single Ni layer was introduced in (1966) [125, 126]. The quadratic dependence of the PHE output voltage on magnetization was demonstrated.

Afterwards, Ky in 1968 reported the PHE in Co, Fe, Ni, and NiFe FM materials with layers thicknesses within 10–150 nm, and a wide temperature range of 77–293 K [120]. The author concluded that the output voltage slightly increases with a decreasing film thickness at low temperature, which was attributed to the increased defects and impurities concentration in the film. Another report by Yau *et al.* [122] discusses the PHE in NiFe alloys with 50%, 80%, and 100% Ni content. The output voltage varies noticeably with the Ni content, and it shows a parabolic dependence on the field for fields above saturation. This result was explained by the existence of an inertial field, the domain structure. The exploitation of PHE to explore the thin films rotational hysteresis, was developed by Vatskichev, *et al* [127], where they concluded that PHE voltage hysteresis area calculations can produce a uniaxial anisotropy magnitude in thin films. Berger [128], displayed that for PHE, the voltage which is proportional to the thickness of domain wall is shaped when the DC current transverses the domains.

Later on, Schuhl *et al.*, fabricated a sensor for low magnetic field detection relying on the PHE principle in ultrathin Permalloy film. A reachable 10 nT detection limit and  $100 \text{ V A}^{-1}\text{T}^{-1}$  sensitivity was acquired [129–131]. A sensor designed for microcompass applications introduced by Montaigne *et al* based on the Permalloy thin film has a reachable

$200 \text{ V A}^{-1}\text{T}^{-1}$  sensitivity and 10 nT detection limit within a 1–1000 Hz frequency [57]. The investigation of the perpendicular anisotropy in Co thin film was also performed using the PHE with a perpendicularly applied magnetic field on the film surface by Ogrin *et al* [132]. The offset voltage is also explained in terms of origin and its suppression tactics. Following up on this, Santos *et al* [96] prepared Permalloy films where they investigated the propagation of the PHE, and concluded that the transverse voltage possesses a strong variation where the field is perpendicular to the films plane. A model to express this was proposed, thus it is convenient for angular positioning. The exchange bias systems with FM/AFM bilayers with the PHE was firstly proposed by Kim *et al* where NiO/NiFe system was used and an optimization of the PHE using biaxial currents was employed [116].

After 1999, Baselt *et al.*, showed a potential detection of biomaterials by using a GMR-based sensor, the PHE is also investigated for the biosensing by several groups [43, 133–136]. It was found that the facile fabrication and unique properties of PHE sensors were very useful in detecting magnetic labels/beads with a very good S/N ratio. Afterwards, these researchers tried to enhance the sensor sensitivity and resolution either by changing the sensor structure [65, 93, 108] or sensor geometry [108, 137]. During these investigations, new sensor application fields have emerged such as current monitoring [137], oil and gas pipeline inspection [44], and non-volatile logic gates functionalization [138]. Recent investigations of PHE sensors have focused on the different sources of noise and thermal stability [94, 139], as well as integration with wearable devices [137, 140, 141]. The implications of sensor structure and sensor geometry on PHE sensor sensitivity is provided in detail under sections 3 and 4. Flexible PHE-based sensors are discussed in section 7. The historical timetable for the evolution of the PHE is displayed in figure 6.

## 3. Effect of sensor structures on PHE sensitivity

In this section, we cover different layers composing the PHE sensors and their correlation with the sensitivity and MR magnitude with more focus on Permalloy based structures of PHE as well as seed and capping layers contributions to the sensitivity.

### 3.1. PHE in a single FM layer

PHE can be observed in the Hall voltage of single layer FM materials [46, 120, 122, 129, 142–144]. When the conditions given in theoretical background (figure 3(a)) have been supplied, the PHE signal exhibits a quite linear region as shown in figure 3(b). This linear region can be used for measuring/detecting magnetic fields in the range of millitesla (mT) and picotesla (pT). In order to detect low magnetic fields down to the pT level, the FM sensing layer must be magnetically soft with a good AMR ratio. Therefore, the FM materials such as NiFe, CoFe and NiCo are good candidates to be a sensing layer

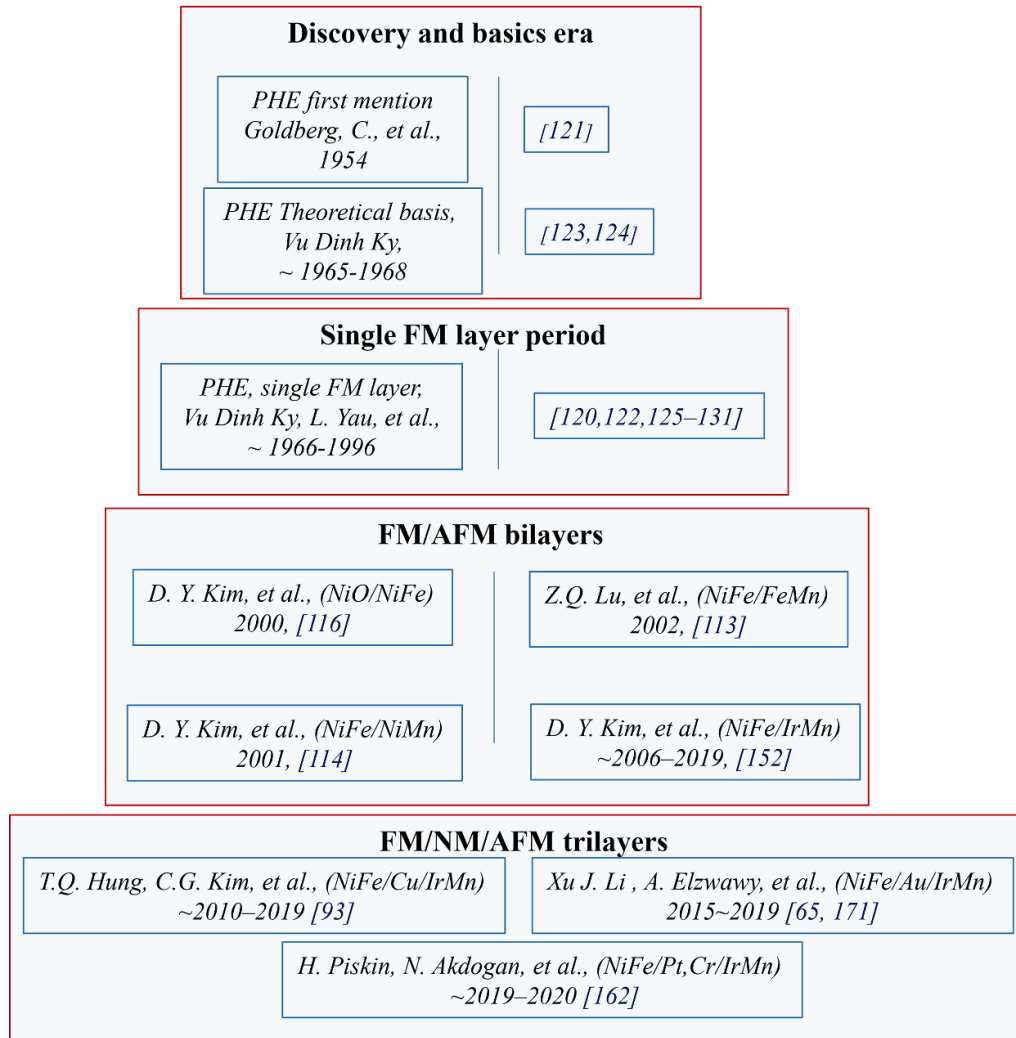


**Figure 6.** The evolution of the planar Hall effect related work with the appropriate timing for each phase, with their related references.

of PHE sensors [108, 110, 145, 146]. Also, the uniaxial magnetic anisotropy property of these materials makes it easier to control the output signal of the PHE sensors for applications. In the FM layers, such as NiFe, the magnetization favors to lie along a particular axis (or several axes) called the easy axis of magnetization, leading to magnetic anisotropy. The application of an external magnetic field on the FM layer causes the rotation of the magnetization from its original direction by an angle  $\theta$ . The values of angle  $\theta$  depend on the value of the external magnetic field and the properties of the FM layer. Applying sufficient magnetic field perpendicular to the easy axis causes the rotation of the magnetization from its original direction  $\theta = 0^\circ$  to the direction of the applied magnetic field  $\theta = 90^\circ$  (usually called the hard axis of the magnetization). The cancellation of the applied magnetic field causes the rotation of the magnetization from  $\theta = 90^\circ$  to  $\theta = 180^\circ$ . When the FM layer is employed as a planar Hall sensor, the voltage corresponding to this rotation (from  $\theta = 0^\circ$  to  $\theta = 90^\circ$  and from  $\theta = 90^\circ$  to  $\theta = 180^\circ$ ) will show a large hysteresis due to the linear dependence of the planar Hall voltage on the

sinus of the angle  $2\theta$  ( $V_{\text{PHE}} \sim \sin(2\theta)$ ). This hysteresis can be avoided by coupling the FM layer to an AF layer which induces a unidirectional anisotropy of the magnetization due to a fundamental interfacial property called the exchange bias interaction.

In the early studies, Dau *et al* have demonstrated that the PHE signal of a single layer of NiFe grown on Fe/Pd buffer can detect low magnetic fields below 10 nT [131]. Recently, Nhalil *et al* have illustrated that the elliptical shaped NiFe layer can detect low magnetic fields down to 5 pT level and they have reported that the micro-structured magnetoresistive sensor based on PHE can be used instead of fluxgate sensor which is larger and more expensive [147]. However, the PHE signal of a single NiFe layer (without an exchange bias field,  $H_{\text{ex}}$ ) exhibits hysteresis due to the switching behavior of magnetization during magnetic field sweeping [57, 131]. Since the hysteresis of the PHE signal is undesirable for many sensor applications, it can be removed by considering exchange biased FM/AF bilayer or double biased FM/AF/FM sensor structures.

### 3.2. Bilayers

The phenomenon of the exchange bias was discovered 63 years ago by Meiklejohn and Bean during their work on nanoparticles of the core-shell structure (Co/CoO) [73]. From a macroscopic point of view, the effect of the exchange interaction between the two FM and AF layers appears clearly in the shift of the hysteresis cycle  $M(H)$  from zero for a single FM layer to non-zero values for the FM/AF bilayer structure. The value of the field shift is called the exchange bias field ( $H_{\text{ex}}$ ). The application of an external magnetic field to the hard axis of the bilayer structure incites the rotation of the magnetization from  $\theta = 0^\circ$  to  $\theta = 90^\circ$  and when the applied field has removed the magnetization of the bilayer structure rotates from  $\theta = 90^\circ$  to  $\theta = 0^\circ$  which eliminates the hysteresis of the planar Hall voltage.

Besides, the exchange bias compels the magnetic moments in the FM layer to rotate coherently towards the applied magnetic field, and by consequence, it improves the thermal stability of the planar Hall sensor and reduces the Barkhausen noise. Due to these advantages, the planar Hall sensor based on a bilayer structure is a good candidate for the detection of small magnetic fields. However, a deep understanding of the effects of the thickness, shape, material compounds, and the size of magnetic layers were required to develop a bilayer planar Hall magnetic sensor that combines high sensitivity, low noise, high thermal stability, and a low limit of detection.

In the FM/AF bilayer or double biased sensor structures, the exchange bias effect induces a unidirectional magnetic anisotropy which results in a reversal behavior of magnetization without switching [91, 145, 148–150]. Thus, the hysteresis behavior of the PHE signal can be removed. In the literature, IrMn material has commonly been used as an AF layer due to its high electrical resistivity and high Néel temperature [151]. Besides, Thanh *et al* and Damsgaard *et al* have worked on the FM thickness dependence of the PHE sensitivity ( $S_{\text{PHE}}$ ) in the bilayer structure of NiFe( $t$ )/IrMn for the thickness ranges between 3–20 nm and 20–50 nm, respectively [43, 152, 153], the similar direction is applied on (NiO (30 nm)/NiFe( $t$ )) bilayer by Kim *et al*, within 5–30 nm thickness [154]. They have observed an increase in  $S_{\text{PHE}}$  as the thickness of the NiFe layer increased. The sensitivity increase in the PHE signal has been explained by considering two main effects:

- (a) the exchange bias field ( $H_{\text{ex}}$ ) has decreased as a function of increasing thickness of the NiFe sensing layer. Thus, the magnetic moments of the NiFe sensing layer can be rotated more freely toward the applied magnetic field which results in higher magnetic field sensitivity.
- (b) the observed resistivity difference ( $\Delta\rho = \rho_{\parallel} - \rho_{\perp}$ ) of the FM sensing layer has increased when the thickness of the NiFe layer is increased. This results in a maximum voltage increase of the PHE signal which provides increased sensitivity. The reported resistivity trends as two regimes, one less than 10 nm NiFe thickness where the resistivity increases, and one higher than 10 nm NiFe thickness

where it decreases. This is explained by the surface interaction contributions in the multilayer, when NiFe is a few nm thickness, IrMn and Ta dominate. For further increase of NiFe thickness, it obtains enough surface contributions to affect and reduce the resistivity magnitude following the Fuchs–Sondheimer theory [153].

However, the strong pinning of the exchange bias interaction in the NiFe/IrMn bilayer system restricts the magnetic field sensitivity ( $S_{\text{PHE}}$ ) of the PHE signal compared to a single NiFe layer. To increase the  $S_{\text{PHE}}$  further, the exchange bias field ( $H_{\text{ex}}$ ) must be further reduced. This can be accomplished by using a trilayer structure of FM/NM/AF or a spin-valve structure of FM/NM/FM/AF.

### 3.3. Trilayers

The exchange bias field ( $H_{\text{ex}}$ ) can be reduced by inserting a NM thin spacer layer between FM and AF layers [93, 97, 155, 156]. Thus, the  $H_{\text{ex}}$  can be well-tuned in FM/NM/AF trilayer sensor structures by varying the thickness of the NM spacer layer. The exchange bias decreases exponentially with the increase of the spacer layer thickness and vanishes around 1 nm thickness while this thickness is enough to completely separate the FM/AF layers [65, 93, 157–161]. In the literature, mostly the Cu material has been used as a spacer layer. When a very thin Cu spacer layer has been inserted between NiFe and IrMn layers, a significant increase in  $S_{\text{PHE}}$  has been observed [93, 112]. However, although the exchange bias field ( $H_{\text{ex}}$ ) can be reduced by inserting a thicker Cu spacer layer, the PHE sensor's sensitivity ( $S_{\text{PHE}}$ ) has not been further increased due to the decreased maximum output voltage of the PHE signal. The decrease in the maximum output voltage of the PHE signal can be explained by recalling the  $V_{\text{PHE}}$  expression given in equation (4). When the sensor structure consists of different layers than the FM sensing layer, the applied current  $I$ , is separated into  $I_{\text{FM}}$  and  $I_{\text{shunt}}$ . Thus, the  $I_{\text{FM}}$  decreases in the presence of other layers (shunt layers) depending on their resistivities. Furthermore, the good conductivity of Cu spacer layer results in a large decrease in  $I_{\text{FM}}$  as the thickness of the Cu layer increased. Therefore, the sensor's maximum output voltage is reduced. In the literature, there are also few efforts to investigate the effect of different types of spacer layers such as Au, Pt, and Cr materials in the trilayer structures of NiFe/NM/IrMn [65, 162–164]. Li *et al* has reported a very good enhancement of PHE sensitivity by using Au spacer layer up to 1 nm thickness. So far the prominent thickness of the spacer layer for sensitivity is around 0.5–0.6 nm [65]. Surprisingly, they have observed a maximum voltage increase despite the Au spacer thickness being increased. This is attributed to the enhancement of resistivity difference ( $\rho_{\parallel} - \rho_{\perp}$ ) of the NiFe layer when it is interfaced with the Au spacer. A similar enhancement of resistivity difference has been observed in the NiFe/Pt/IrMn sensor structure by Pişkin *et al* using a Pt spacer layer up to 1 nm [162, 165]. This indicates that both Au and Pt spacer layers repair the negative effect of Cu. Thus, the  $S_{\text{PHE}}$  can be further increased in NiFe/NM/IrMn (NM: Au, Pt)

trilayer structures compared to the NiFe/Cu/IrMn structure. Moreover, Elzawy *et al* have reported that the power consumption of PHE sensors can be minimized without sacrificing sensitivity [100]. In their study, equisensitive PHE sensors have been successfully fabricated by varying the thicknesses of spacer and capping layers. It is shown that the output voltage of the PHE sensor can be tuned by varying the thickness of capping layer, while the exchange bias field ( $H_{ex}$ ) can be tuned by adjusting the thickness of the spacer layer.

In connection with the use of Au and Pt layers, we can mention a special class of structures of the type FM/HM where a large spin Hall MR (SMR) can appear [1–3]; HM represents a heavy metal thin layer like Pt,  $Au_xPt_{1-x}$  alloy [166], W [167], PtHf and PtAl alloys [168] or Pt/Hf multilayer [169] whereas FM is a FM layer like NiFe, CoFeB [166–168]. When the current flows through the multilayered structure, the NM layer acts as a spin orbit torque (SOT) biasing layer [166–168] for the FM layer. The current-induced magnetization due to SOT effect eliminates the need of a biasing field from an external source or from an exchange coupling with an AF layer. We must note that SMR is based on the spin Hall effect (SHE) and on the inverse SHE (ISHE) in NM [167]. A typical PHE setup is used for sensing applications with such structures [166, 167]. Using a Wheatstone bridge comprising of four ellipsoidal NiFe(2.5 nm)/Au<sub>0.19</sub>Pt<sub>0.81</sub>(3.2 nm) sensing elements with a long axis length of 800  $\mu\text{m}$  and short axis of 200  $\mu\text{m}$ , a SMR sensor with nearly zero DC offset and negligible hysteresis was reported in [166]. The sensitivity is up to 1.10 mV V<sup>-1</sup> Oe<sup>-1</sup> at 20 °C within a linear region of  $\pm 0.86$  Oe and the field detectivity can reach 0.71 nT Hz<sup>-1/2</sup> at 1 Hz. Despite the simplicity of such structures, work has to be done on HM and FM layers to increase the SMR effect, the linear range and to improve the stability of the sensitivity with temperature [166, 170]. Also, it must be noted that PHE setup or the Wheatstone bridge configuration can also be used to characterize SOT effective fields and the MR effect in FM/HM structures.

Another improvement in the NiFe/Au/IrMn trilayer based PHE sensors has been introduced by substituting the Ta capping layers with NiFeCr layer [171]. When the NiFeCr material has been used instead of Ta capping layer, a better condition for domain wall pinning in the NiFe sensing layer has been observed. This results in a lower value of Barkhausen noise. Thus, a 50% higher S/N ratio has been reported compared to a sensor structure that contains the Ta capping layer. Besides, it is important to mention here that the higher S/N ratio enables the detection of lower magnetic fields.

Recently, Mahfoud *et al* have presented a very interesting method to stabilize the magnetic field sensitivity of PHE sensors by using a trilayer sensor structure of NiFe/Cu/IrMn in an unstable thermal environment [94]. In this study, they have found a special case that the sensor's magnetic field sensitivity does not significantly change with varying temperature. It has been reported that the PHE sensors with the thermal stability of sensitivity can be used for the characterization of low volume and low dimension magnetic materials like single molecular magnets. The NiFe thickness effect is explained as well for NiFe/Cu/IrMn trilayer structure with a varied NiFe thickness 10–30 nm and Cu thickness 0–0.6 nm, in summary,

20–30 nm thickness of NiFe accompanied by 0.6 nm thickness of Cu layer gives around 90% elevated signal [172], few reports interconnect with AF materials conjugated with NiFe for PHE sensors [113, 114] However, up to the authors best knowledge, no IrMn layer thickness effect on PHE sensors is investigated in this bi- and tri-layer structures.

### 3.4. Spin-valves

The spin-valve structure typically consists of two FM layers separated by a NM conducting (spacer) layer. It is important to note that when the thickness of the spacer layer is smaller than the mean free path of the electrons, the two FM layers can affect each other via Ruderman–Kittel–Kasuya–Yosida (RKKY) interaction. The RKKY interaction between two FM layer is known to cause a unidirectional magnetic anisotropy when one of the FM layers is pinned by an AF layer. Thus, the other almost free FM layer can be used as sensing layer for PHE sensors [110, 173–177]. The RKKY interaction can also be used to tune the  $H_{ex}$  of the NiFe sensing layer by varying the thickness of a spacer layer or varying the thickness of FM layers. In order to optimize the magnetic field sensitivity of spin-valve based PHE sensors, Hung *et al* has investigated systematically the effect of thickness of FM free ( $t_f$ ) layers in Ta(5)/NiFe ( $t_f$ )/Cu(1.2)/NiFe (2)/IrMn(15)/Ta(5) (nm) ( $t_f = 4$ –16 nm) structure [178]. They have observed a sensitivity increase as the  $t_f$  increased up to 16 nm. However, the magnetic field value of the peak in PHE signal did not change a lot as the  $t_f$  was increased. Thus, they have explained the enhancement of sensitivity by decreasing the shunt current from other layers. A similar systematic study has been done by Tu *et al* considering the effect of thicknesses of the FM pinned ( $t_p$ ) and the FM free ( $t_f$ ) layers in Ta(5)/NiFe ( $t_f$ )/Cu(1.2)/NiFe ( $t_p$ )/IrMn(15)/Ta(5) (nm) ( $t_f = 4$ –26 nm,  $t_p = 1$ –12 nm) structure [179]. They have observed the same shunt current effect with similar magnetic anisotropy behavior when the  $t_f$  varied in the working range. In addition, they have reported that the PHE sensor sensitivity increases as the thickness of  $t_f$  increased and  $t_p$  decreased. Thus, the highest PHE sensitivity has been reported in the spin-valve configuration with  $t_f = 26$  nm and  $t_p = 1$  nm.

### 3.5. Seed and capping layer effect

The seed layer in general affects the MR ratio [149] as a better-smoothed seed layer promotes a lowered grain boundary and a larger grain size that increases (111) texture for the subsequent layers. This leads to a longer mean free path affected by scattering of the conduction band electrons and finally, an elevation of the MR value can be noticed. According to Wang *et al* the optimum MR ratio value (3.5%) of the seed layer was at  $\approx 5$  nm thickness and 400 °C for Ta as the most commonly used seed layer with the Permalloy FM layer [180], whereas the NiFeCr was found as a superior alternative for Ta seed layer [181–185]. Contrary to the Ta seed layer which encounters a thermally preferred interaction between Ta and NiFe leading to a magnetically dead layer and a reduced magnetic moment magnitude, NiFeCr does not experience this

interaction. The  $(\text{NiFe})_{1-x}\text{Nb}_x$  seed layer is also used and has a reported 3.76% MR ratio at  $x \approx 20\%$  of NiFeNb alloy at 450 °C, while Ta has a 3.27% MR ratio at the same conditions [186, 187]. The capping layer effect in general is a protective layer of the humidity and surroundings. Vastly, the capping layer affects the overall resistance of the stacking which subsequently affects the effective output voltage [188], of the sensors. Lately, another point of view on the capping layer contribution is discussed and depicted [171], in terms of the mechanical energy changes. A threefold elevation of the exchange bias value is maintained upon introducing a NiFeCr capping layer in contrast with the usual Ta layer. Since the collision probability of sputtered atoms with different masses, a change in momentum transfer can be acquired. The transfer is linked to coupled/decoupled areas in the FM/AF interface leading to the increase in exchange bias magnitude.

#### 4. Effect of the sensor geometry on PHE sensitivity

The PHE sensors are patterned with different geometries in relation to the desired application. The most usual geometries are: cross-shaped, elliptical, and disk-shaped. Other geometries, which mimic the PHE, exist as ring shaped or diamond shaped AMR resistors connected in a Wheatstone bridge. These resistors are named PHE bridge (PHEB) and, to sustain the correct orientation of the magnetization inside of these arms, an exchange-biased stack is used [137]. Some results regarding the development of Permalloy based PHE sensors are presented as follows.

##### 4.1. Cross junctions

Theoretically, the PHE voltage does not depend on the length or width of a cross junction, but is affected by the thickness of the FM layer as expressed in equation (4). Until the year ~2010 the planar Hall sensors were manufactured based on cross-shaped architectures. The widespread use of this shape is due to the ease of its manufacture as well as the existence of a large body of research that has studied the various magnetic interactions occurring in these shapes. Also, these shapes appeared to be an appropriate option for some technological applications especially those related to biological detection as increasing the active surface of the sensor could increase the possibility of detecting biological molecules. Hung *et al* has experimentally investigated the effect of cross size on the PHE voltage by fabricating a spin-valve structure of Ta(5)/NiFe(6)/Cu(3)/NiFe(3)/IrMn(15)/Ta(5) (nm) with the cross sizes of  $50 \times 50 \mu\text{m}^2$ ,  $50 \times 70 \mu\text{m}^2$  and  $50 \times 100 \mu\text{m}^2$  [189]. They have observed the same PHE voltage profiles when the cross size has been varied. A similar experimental study has been carried out by Donolato *et al* They have fabricated a bilayer structure of Ta(3)/NiFe(30)/IrMn (20)/Ta(3) (nm) with the cross sizes varied between  $40 \times 40 \mu\text{m}^2$  and  $3 \times 3 \mu\text{m}^2$  [190]. They have observed the same PHE voltage profiles when they used the  $40 \times 40 \mu\text{m}^2$  and  $20 \times 20 \mu\text{m}^2$  crosses. This finding was very similar to the results observed by Hung *et al* However, when the cross size

has been reduced below  $10 \times 10 \mu\text{m}^2$ , they have observed hysteresis in the PHE voltage profile with an increasing trend. They have investigated this hysteresis behavior of the PHE signal by taking a magnetic force microscopy (MFM) images of crosses and by micromagnetic simulations. They concluded that when the cross size is reduced a new magnetic easy axis has occurred due to the shape anisotropy. The presence of a new easy axis has resulted in a hysteresis behavior in the PHE voltage profile. The importance of this work lies in highlighting the effect of the sensor's dimensions on its magnetic behavior, especially for magnetic sensors that have small dimensions. The low dimensional sensors could be the next generation of planar Hall magnetic sensors due to the urgent need to reduce the size of the sensor to detect small magnetic materials. In another study, Hung *et al* have successfully fabricated a spin-valve structure of Ta(5)/NiFe(16)/Cu(1.2)/NiFe(2)/IrMn(15)/Ta(5) nm with a cross junction size of  $3 \times 3 \mu\text{m}^2$  [174]. But they have reported no hysteresis in the PHE voltage profile. It is well understood, when the exchange anisotropy is well enough to overcome the shape anisotropy, the PHE signal does not exhibit hysteresis. These investigations have shown that the cross junctions can be successfully fabricated in different sizes according to the requirement of an application.

For the cross junctions, if a single FM layer, like a NiFe material, has been used, several tens of  $\mu\text{V} (\text{Oe}\cdot\text{mA})^{-1}$  PHE sensitivity can be obtained [57, 131, 146]. However, the exchange biased sensor structures (bilayer, trilayer and spin-valve) can provide a sensor sensitivity typically some of  $\mu\text{V} (\text{Oe}\cdot\text{mA})$  due to the presence of exchange bias field ( $H_{\text{ex}}$ ) and increased shunt current ( $I_{\text{shunt}}$ ).

In [129, 131], early results in microfabrication of high sensitivity PHE sensors, with a sensitivity of 100 V/AT and a minimum detectable field below 10 nT were reported. The sensing layer consists of Permalloy and is 6 nm thick, epitaxially grown by molecular beam epitaxy. Uniaxial magnetic anisotropy is induced in the film through FM coupling with a Fe/Pd bilayer epitaxially grown on MgO (001). A large enhancement of the PHE sensitivity was reported in a NiO/NiFe/NiO heterostructure figure 7 [92].

This sensitivity improvement derives from (a) the increase of resistivity change ( $\Delta\rho$ ) and (b) the decrease of the saturation field ( $H_{\text{sat}}$ ). A sensitivity up to  $1200 \text{ V A}^{-1}\text{T}^{-1}$  was reported in this study for an optimal stack of the type Ta(5)/NiO(3)/NiFe(8)/NiO(2)/Ta(3 nm). This remarkable enhancement of the sensitivity is strongly related to the strengthened electron scattering by the flat oxide/metal interfaces and the easier magnetization rotation because of the reduced intermixing of Ta and NiFe [92].

In [191], the PHE in NiFe films was studied using MgO as the buffer and capping layer in order to reduce the shunt effect. A sensitivity of about  $865 \text{ V A}^{-1}\text{T}^{-1}$  was reported in a MgO (3 nm)/NiFe (5 nm)/MgO (3 nm)/Ta (3 nm) structure after thermal annealing at 500 °C 2 h<sup>-1</sup>. After this annealing smooth MgO/NiFe and NiFe/MgO interfaces were found and the shunting effect due to Ta layer was decreased. The smooth interfaces lower the diffusive scattering of electrons at MgO/NiFe and NiFe/MgO interfaces.

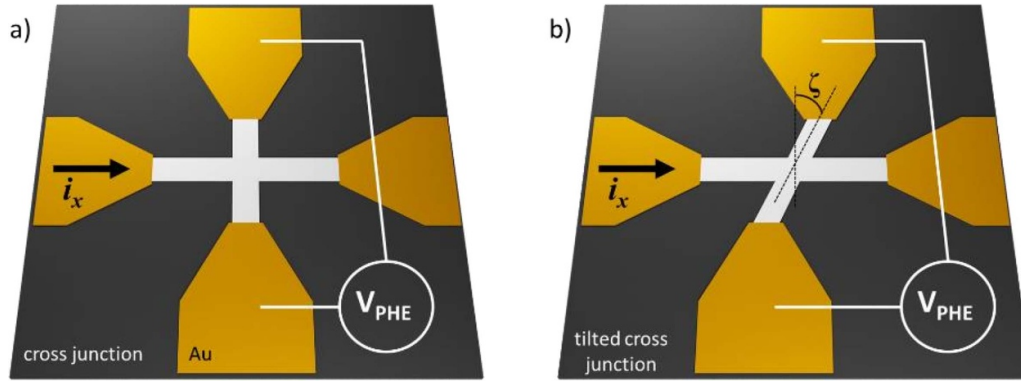


**Figure 7.** (a) Typical cross-shaped Permalloy based PHE sensor (reproduced from [64]. CC BY 3.0.), and (b) tilted cross junction as sketched in [189] (reproduced from [189]). © IOP Publishing Ltd. All rights reserved).

4.2. Tilted-cross junctions

The main idea behind the fabrication of tilted-cross junctions is to combine the longitudinal MR effects such as AMR, GMR with the PHE which is the transverse AMR component [189, 192]. This combination of MR effects in one sensor remarkably increases the magnetic field sensitivity compared to a cross junction fabricated with the same sensor structure. Hung *et al* have systematically investigated the sensor’s magnetic field sensitivity in  $100\ \mu\text{m} \times 50\ \mu\text{m}$  crosses fabricated with a spin-valve structure of Ta(5)/NiFe(6)/Cu(3)/NiFe(3)/IrMn(15)/Ta(5) (nm) by varying the tilt angle between  $0^\circ$  and  $45^\circ$  [189]. They have observed that the magnetic field sensitivity has been gradually increased as the tilt angle changed to  $45^\circ$ . Furthermore, they reported that this tilted configuration exhibited not only better sensitivity, but also better linearity as compared with the typical PHE cross junction sensor. It is important to note that the shape of the output signal of the tilted cross junctions changes due to the contribution of other MR effects. Therefore, the working range (linear region) of this type of magnetic field sensor shifts. In sensor applications of tilted cross junctions, this shift of linear region must be considered.

4.3. Bridge junctions

A very interesting development of the PHE sensor has been realized by replacing the traditional cross junction with a Wheatstone bridge design by using the exchange biased bilayer, trilayer, and spin-valve sensor structures [103, 108, 193–199]. Since the output voltage characteristic for this configuration of the Wheatstone bridge has the same angle dependence of magnetization as the PHE signal of cross junctions, they were termed PHEB sensors to distinguish them from other types of AMR bridge sensors. Figures 8(a)–(d) present diamond-shaped and ring-shaped bridge sensors, respectively [193, 194], where  $l$  is the length, and  $w$  is the line width of the resistor elements. It is important to mention that, the exchange bias and anisotropy fields have been aligned along the  $x$ -axis and the magnetic field has been applied along the  $y$ -axis. The constant current of  $i_x$  has been applied from the  $a$ – $b$  terminals and the voltage has been recorded from the

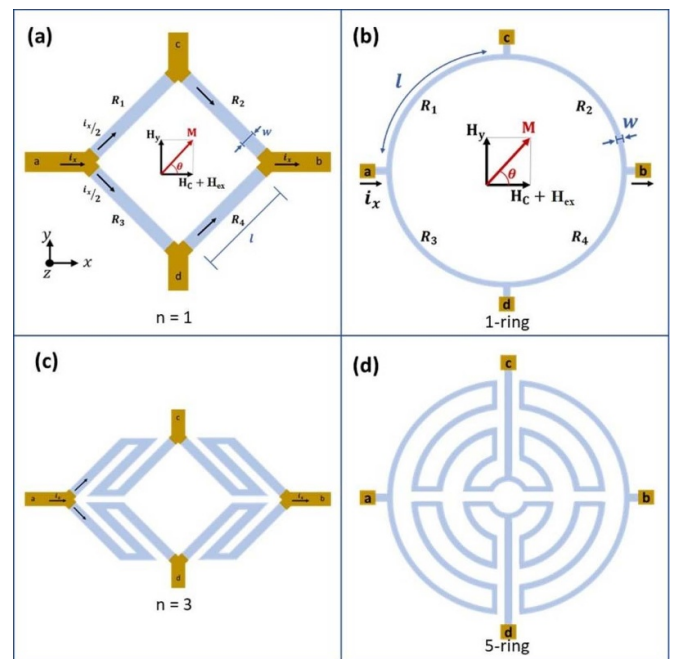


**Figure 8.** PHE bridge designs in diamond-shaped (a), (c) reprinted from [193], with the permission of AIP Publishing, and ring-shaped (b), (d) geometries reprinted from [194], Copyright (2011), with permission from Elsevier.

$c$ – $d$  terminals. For this configuration of Wheatstone bridges, a magnetic field profile of PHE signal given in figure 3(b) can be obtained.

The output voltage of the Wheatstone bridges should be well understood before proceeding with the findings of the experiments. The output voltage of a Wheatstone bridge ( $V_{\text{out}}$ ) can be expressed by the following function when the bridge has been biased with a constant current of  $i_x$  [200]:

$$V_{\text{out}} = i_x \frac{R_2 R_3 - R_1 R_4}{R_1 + R_2 + R_3 + R_4} \quad (7)$$

where the  $R_1, R_2, R_3$  and  $R_4$  stand for the resistance elements of the Wheatstone bridge, which is produced by using an exchange biased PHE sensor structure. It is important to note

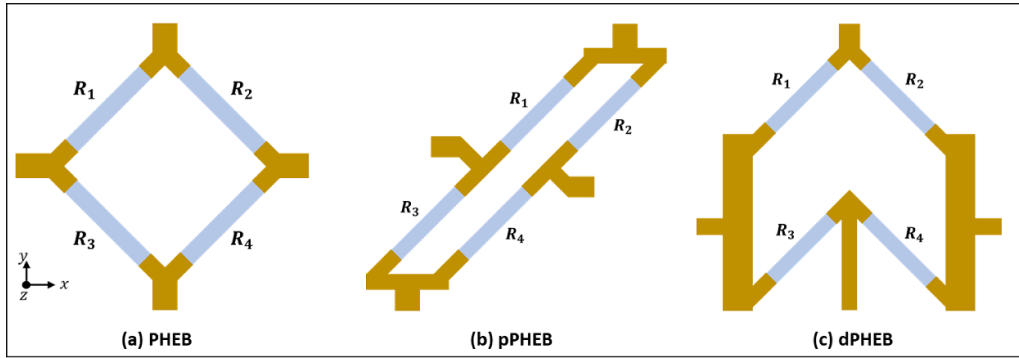


**Figure 9.** Wheatstone bridges with different configurations. (a) PHEB (b) parallel-PHEB (pPHEB) (c) differential-PHEB (dPHEB) reprinted from [200], with the permission of AIP Publishing.

that the  $R_1 = R_4$  and  $R_2 = R_3$  when the PHEB has been symmetrically designed by using a diamond or ring shape. If this condition replaced into equation (7), the  $V_{\text{out}}$  can be written in the following form:

$$V_{\text{out}} = \frac{i_x}{2} (R_2 - R_1). \quad (8)$$

It is very clear that the  $V_{\text{out}}$  is not zero when a difference has occurred between  $R_2$  and  $R_1$  resistances. In addition, the resistance elements ( $R_1$  and  $R_2$ ) of a diamond shape can be expressed individually by considering the AMR properties of FM materials as follows:

$$R_{\theta} = \frac{l}{wt} [\rho_{\perp} + (\rho_{\parallel} - \rho_{\perp}) \cos^2 \theta]. \quad (9)$$

If equation (9) replaced into equation (8), the  $V_{\text{out}}$  will be related to the  $(l/w)$  ratio.

In early studies of PHEB sensors, Henriksen *et al* and Oh *et al* have experimentally and theoretically demonstrated that the sensor's output voltage can be enhanced by a geometric factor of  $(l/w)$  [193, 194]. Thus, the magnetic field sensitivity of PHEB sensors can be largely enhanced when the  $(l/w)$  has been increased. In the study of Henriksen *et al*, they have fabricated an exchange-biased bilayer structure of Ta(5)/NiFe(30)/IrMn(20)/Ta(5) (nm) with various size of Wheatstone bridges in a diamond shape [193]. When the geometric factor of  $(l/w)$  has been experimentally tuned as 20 with the  $n = 7$  repeats (which means  $l/w = 140$ ), they observed a 102 times improvement in the sensitivity compared to the cross junction fabricated with the same sensor structure. The detectability of the planar Hall sensor in low-frequency regime was improved by one order by using the bridge geometry instead of using the cross geometry [195]. Furthermore, it has been reported that the magnetic field sensitivity of PHEB sensors can be further increased by altering the sensor structure with a lower exchange biased one such as the spin-valve or the trilayer sensor structures [193, 194, 197].

Parallel to the development of the bilayer bridge sensor, another development in the geometry of the bilayer planar Hall sensor which was based on ring architecture was proposed by

Kim's group [201]. Ring architecture bilayer sensors with differing width ( $w = 5 \mu\text{m}$  and  $10 \mu\text{m}$ ) and radius ( $r = 30 \mu\text{m}$ ,  $60 \mu\text{m}$ ,  $90 \mu\text{m}$ , and  $120 \mu\text{m}$ ) and multiring sensors were investigated. These studies showed that the sensitivity and the output voltage of the sensor increase with the increase of the radius of the ring and/or with the decrease of the width of the ring. Additionally, the study showed that the sensitivity and the output voltage increase with the number of rings also. A high sensitivity of the multiring sensor of  $3.3 \text{ mV mT}^{-1}$  was achieved for the multiring sensor compounded by seven rings with a width of  $5 \mu\text{m}$ . This sensitivity was improved when the magnetic field was applied with an angle of  $20^\circ$  to the easy axis, the sensitivity of the multiring sensor at this angle increased 2.5 times. For example, the use of NiCo FM layer as a sensitive layer instead of NiFe for planar Hall sensor based on the ring shape was introduced, which improved the signal voltage and the dynamic range of the sensor [108]. When compared to the ring geometry, the diamond geometry has been found theoretically 41%, and experimentally 30% more sensitive to the low magnetic fields [137]. The difference between theory and experiment has been explained as the diamond shaped sensors can be more affected by demagnetization effects than ring sensors. As a result, both the diamond and ring designs of bridge sensors have largely enhanced the magnetic field sensitivity and seemed to offer higher performance levels compared to those provided by the conventional cross junction PHE sensors.

In another study, Østerberg *et al.*, have provided and optimized two more configurations of PHEB sensor which is shown in figure 9. They have termed the new Wheatstone bridge designs as parallel PHEB (pPHEB) and differential PHEB (dPHEB) sensors [200, 203]. It is evident that the  $(R_2 R_3 - R_1 R_4)$  term in equation (7) is always zero for the pPHEB and dPHEB sensor designs. Therefore, the pPHEB and dPHEB sensor designs are not sensitive to the homogenous external magnetic fields, unlike the PHEB. But these sensors can provide a signal caused by only the MNPs when one of the resistance elements has been used for the sensing. Furthermore, in the pPHEB design, the sensor's self-fields (Oersted fields) caused by the applied current is additive due to the parallel shape of the sensor. It has been demonstrated that the sensor's self-fields can also be eliminated in dPHEB design.

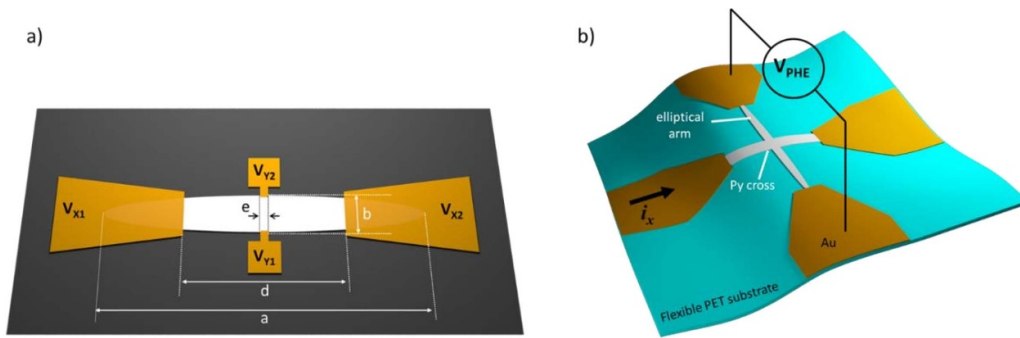


**Figure 10.** (a) Elliptical shaped Permalloy based PHE sensors deposited on rigid substrate reprinted from [202], with the permission of AIP Publishing, and (b) on flexible substrate reproduced from [47]. CC BY 4.0.

Besides, Henriksen *et al* have reported that the sensor's self-field (Oersted field) due to the applied current can also be used to detect the MNPs [172, 198]. This allows MNP detection without the need for external magnetic fields. With these fascinating properties of bridge junctions, they have been found very promising in many sensor applications.

#### 4.4. Elliptical-shaped PHE sensors

A straightforward method to keep the initial orientation of the magnetization along the current direction is to microfabricate elliptical-shaped Permalloy based PHE sensors with a very large aspect ratio 10:1 (figure 10(a)) to induce a preferred magnetization axis can be induced by the shape anisotropy. In [47] was reported such a sensor deposited on polyethyleneterephthalat (PET) substrate, figure 10(b) with a sensitivity of  $0.86 \text{ V T}^{-1}$ , for a bias current of 5 mA, and a detection limit of 20 nT. Such a sensor presents, also, the ability to work as a rotation sensor, as we showed in figures 3(c) and (d). PHE sensors deposited on flexible substrate can be used in the field of flexible electronics with applications in health monitoring. Using the same geometry of elliptical shape PHE sensor (5 mm long axis and 0.625 mm short axis), but integrated within flat trapezoidal magnetic field concentrators, a 5 pT magnetometer at room temperature has been reported [147].

In [62], disk-shaped structures were used to microfabricate Permalloy based PHE sensors. Because no anisotropy axis is defined in this case, a biasing field was used to align the magnetization parallel with current direction when the applied field is zero. Sensitivity up to  $6 \mu\text{V} (\text{Oe.mA})^{-1}$  was found for a field range of about  $\pm 10 \text{ Oe}$ . The superb linearity of the measured signal for  $H_{\text{ex}}$  higher than 25 Oe suggests that the main mechanism of the magnetization reversal processes is based on the magnetic moment's rotation.

However, the main application for which these sensors were microfabricated is devoted to MNPs detection using the surface-based detection technique [62]. The choice is motivated by the relatively *large detection area*, typical for this geometry, large S/N, and a superior thermal stability. For these sensors, the detection technique is based on *localized reversal nucleation induced by MNPs in the sensing layer*. Such a method was studied, also, for GMR sensors.

Micromagnetic simulations and experiments were conducted in order to increase the dynamic range of these sensors, in terms of MNPs detected [56]. It was shown that micrometre sized structures, with large aspect ratio, have a limited dynamic range, which affects their applicability [56].

In the sensing setup presented in [46], a magnetic field,  $H_{\text{ex}}$ , up to 100 Oe, which is used to polarise the MNPs, is *applied perpendicular* to the sensor surface. By this, can be increased the amplitude of the magnetic field generated by the MNPs *without the risk to saturate the sensor* which is less sensitive to perpendicular fields. A second external magnetic field, *scanning field H*, no larger than 30 Oe, is applied *in the film plane along the sensor's driving current, I*. It was found that the presence of the MNPs above the sensor surface affects the magnetization switching behavior of the sensing layer, therefore, a change in the amplitude of the output signal can be observed. These changes of the output signal occur at *small applied fields H*, between 6 and 10 Oe. Maghemite nanoparticles, 10 nm in diameter, functionalized with PEG 6000 were used for experiments, and detection sensitivities, up to  $0.116 \times 10^{-3} \text{ emu mV}^{-1}$ , can be achieved.

#### 4.5. Impact of junction dimensions ( $l/w$ ) on sensor performance

Another factor that impacts the performance and figure of merits of the PHE sensor is the junction dimensions, (i.e.  $l/w$  ratio). A higher ratio of  $l/w$  around ten conjugated with less thickness of NiFe FM layer for cross shape, leads to triple increase of sensitivity, attributed to shape anisotropy elevation as reported [53]. Different square, rectangle, rhombus and circle Permalloy films are introduced with a varied length to width ratio from 1 to 29, where square shape shows the maximum sensitivity [204, 205]. The impact of the width of the junction arm is stipulated in terms of shape anisotropy. Briefly, PHE is studied with a varied width, for larger magnitude, a hysteresis free accompanied by a single domain model is acquired. While, for smaller width, a remarkable hysteresis behavior is introduced to the sensor profile and magnetization reversal occurs as one step [190, 206, 207]. Moreover, a tilting angle of the cross junction by  $45^\circ$  can raise the sensor sensitivity by 30% [189]. An earlier work demonstrated the PHE in NiO/NiFe bilayer system with a changed width of the junction from 200–400 nm.

The exchange coupling magnitude possesses a reversal proportionality with the arm width for all changed temperatures within 5–300 K. This suggests that the sensitivity is higher for larger width [117]. Attention is also paid to the Wheatstone bridge configuration: as the ratio of  $l/w$  is increased, the output profile curves are noticed to alter by a scaling factor with a linear dependence of sensitivity on this ratio, and depict insignificant hysteresis, a slight voltage offset increase is also observed. In general, a 100× sensitivity elevation is obtained for the bridge topology in comparison with the conventional cross junction [193]. An increased sensitivity aligned with reduced noise is gained with the higher length to width ratio along with a higher repeated number of the meander-like resistor in the bridge configuration [195].

## 5. Thermal drift and noise

Thermal stability and thermal drift for the sensors are vital parameters for operation and integration onto devices. Temperature constancy performance features for AMR and PHE sensors are controlled by double kinds of drifts: baseline drift and signal amplitude fluctuation. As reported by Jeon *et al* [103], the significance of PHE sensors performance relative to AMR is explained within the 25 °C–90 °C range for NiFe/IrMn bilayer structure. The thermal drift is three orders of magnitude lower in PHE than AMR. Limited thermal dependence of the sensitivity in planar Hall sensor is also demonstrated. Mahfoud *et al* [94], attributed the achievable stability of the sensitivity by controlling the interplay between the usual exchange bias, Zeeman energy, and anisotropy energy as a function of the temperature of the sensor. Manifested high thermal stability for NiFe/Cu/IrMn trilayer structure is amongst ±2 mT applied magnetic field magnitude with an extremely low variation of sensitivity of about  $4.5 \times 10^{-3}$  V/A/T/K for an extensive temperature span of –163 °C–86 °C. In addition, the change of the temperature during the biosensing process may affect the sensitivity of the sensor. Damsgaard *et al* studied the thermal behavior of the bilayer planar Hall sensor in the range of temperature between 10 °C and 70 °C corresponding to the typical change of temperature in the biological environment [151]. The temperature coefficient of the sensitivity at room temperature shows a relatively high value of 0.32%/°C. The approach proposed for solving this problem involves the use of a second PHE sensor as a reference sensor to correct the drift of the sensitivity.

Although PHE sensors, fabricated from Permalloy thin films, have been long studied [87, 88, 129, 131], they still have the potential to generate more applications with valuable results [47, 53, 57, 62, 94]. For the thermal stability studies, usually, the PHE sensors have a cross-shaped geometry investigated, but other geometries that allow a specific control of the magnetic properties in the sensing layer can be found [47, 56, 62]. As shown in the previous section, the PHE, which is a consequence of the AMR effect, comes with some advantages like linear behavior around zero field, figure 4(b), and the native equivalent electrical behavior like a Wheatstone

bridge which brings higher thermal stability. The temperature drift appears to be the main factor limiting the low field performance of magnetoresistive detectors where the voltage is measured along the current. Instead, the PHE is actually a measurement of the transverse magnetoresistivity, figure 3. The transverse measurement is sensitive only to the anisotropic part of the resistivity. The suppression of the term  $j_x \rho_{\perp}$  from AMR expression  $E_x = j_x \rho_{xx} = j_x \rho_{\perp} + j_x (\rho_{\parallel} - \rho_{\perp}) \cos^2 \theta$  [83] in PHE setup leads to a drastic reduction, with at least four orders of magnitude, of the thermal drift for a Permalloy based sensor [129, 131]. Such that, nano-Tesla sensitivity can be achieved in the low-frequency range [47, 64, 129].

Noise is an important parameter that can affect the low field detection limit of the MR sensors. Such that, we can enumerate the noises, typically associated with MR-based sensors: thermal noise (Johnson noise), shot noise, and  $1/f$  noise [47, 61, 64]. Thermal noise arises from thermal fluctuations of electrons and is given by the Nyquist formula [195]:

$$S_{\text{Johnson}} = 4k_B T_{\text{abs}} R. \quad (10)$$

With  $k_B$  being the Boltzmann constant,  $T_{\text{abs}}$  the absolute temperature and  $R$  the resistance under test. Thermal noise has no magnetic origin which is independent of the applied voltage but directly associated with the electrical resistance of a sensor. For AMR, GMR and TMR sensors,  $R$  is larger than  $R_y$ , which is the resistance between the measurement arms where PHE is measured; usually  $R_y$  is in the range of tens to hundreds of ohms. If  $R_y = 100 \Omega$ , the thermal noise is  $\sim 1.3 \text{ nV} (\text{Hz}^{1/2})^{-1}$  at 300 K that is equivalent with a magnetic field noise of  $1\text{--}1.5 \text{ nT} (\text{Hz}^{1/2})^{-1}$  [47, 94]. This noise level is much lower than the noise of signal conditioning circuits.

Shot noise is important in MTJs where the existence of an insulating barrier produces discontinuities in the conduction path. Shot noise is expressed by [208]:

$$S_{\text{Shot}} = 2qIR^2 \quad (11)$$

where  $q$  is the electron charge,  $I$  is the current through the structure and  $R$  is the resistance between the measurement contacts.

This term is lower in AMR and GMR but virtually absent in PHE structures.

However, an important component of noises of MR sensors is given by  $1/f$  noise which has a major contribution on low-frequency signals. For example, in magnetic materials, this noise comes from the fluctuations of energy around equilibrium due to the presence of magnetic domains; their movement in Permalloy films can be thermally activated or by mechanical stress induced through vibrations in substrate. The dynamics of magnetic domains are dependent on the sensor shape, size and materials properties [61]. A larger effective anisotropy field due to crystalline anisotropy, uniaxial induced anisotropy, and an exchange biasing field [93], and/or a high aspect ratio of the sensor (shape anisotropy) can bring the sensing layer close to a single domain state. However, a larger anisotropy has the cost of a lower sensitivity. Sensors that exhibit

**Table 1.** The comparison of the most common magnetoresistive sensors (Reproduced from [64]. CC BY 3.0).

Sensor type	$I$ (mA)	Resolution $\mu_0 H_{\min}$ (nT)	Signal to noise ratio (S/N)
Spin valve	10	54	442
Planar Hall effect (PHE)	10	32	1453
Anisotropic magnetoresistance (AMR)— ring	10	26	50
Giant mag- netoresistance (GMR)	5	93	382
Magnetic tunneling junction (MTJ)	1	202	114

hysteresis show much higher field sensitivity [80], so a compromise must be chosen in accordance with the application envisioned. The  $1/f$  noise of the current source can have, also its own contribution, but this can be lower in the case of PHE sensors because of the equivalent differential setup. Using low noise electronics, and integration time up to 10 s, the detection limits can reach levels of nT.

In [64] the main detection characteristics for AMR, GMR, PHE and TMR sensors for MNPs detection are compared. Some useful data adapted from [64] is summarized in Table 1.

The comparison results show that the PHE used for sensing applications has many advantages over others such as a very high S/N and a very high ( $\mu_0 H_{\min}$ ) in the detection of the magnetic field. Furthermore, the voltage profile of a PHE sensor responds linearly to the magnetic field at the small values and the thermal drift of the output signal is better than for other sensors as we stressed above.

## 6. Comparison of the PHE sensitivity

Hung *et al.*, compared the PHE sensitivity for a bilayer of Ta(3)/NiFe(10)/IrMn(10)/Ta(3), a trilayer of Ta(3)/NiFe(10)/Cu(0.12)/IrMn(10)/Ta(3) and a spin-valve of Ta/NiFe(10)/Cu(1.2)/NiFe(2)/IrMn(10)/Ta(3) structures [93]. It is worth noting that the thickness of the NiFe sensing layers has been chosen as 10 nm in all sensor structures. Among these, the highest PHE sensitivity has been obtained from the trilayer structure. They have reported that the magnetic field sensitivity of the trilayer is about one order larger than the bilayer and two times greater than the spin-valve structure. They explained this result as the trilayer structure has the advantages of weak exchange coupling and the high active current passing through the FM sensing layer due to the very thin Cu spacer layer. Thus, the trilayer structure of NiFe/Cu/IrMn has overcome the disadvantages of the bilayer and spin-valve structures resulting in the highest PHE sensitivity. It is stressed that the PHE sensitivity of the trilayer structures can be further increased by using the Au and Pt spacer layers since

both enhance the maximum output voltage of the PHE signal unlike the Cu spacer. The comparison of most familiar PHE structures is delivered in Table 2. Figure 11 represents a visualization of the acquired sensitivity with altered junction geometry.

In this literature, in addition to the structural and geometrical effects on PHE sensor, several studies can be found that investigate the substrate effects [210], etching effects [211], exchange bias field direction dependence [212], magnetization angle dependence [213], reversible and irreversible temperature-induced changes [214], and so on. [112, 188, 215, 216].

## 7. Applications

Systems for the detection of biomolecules are presently moving towards LOC devices that often integrate the sensing of magnetic micro/nano-sized particles within a microfluidic environment. In these systems, the MNPs are functionalized to serve as carriers or labels for the biomolecules, and they provide a magnetic stray field. The latter can be detected by sensors that need to be integrated in the microfluidic environment. Thus, the combination of such sensors with microfluidics is a longstanding topic for research on LOC systems for various applications, as with medical diagnostics or food testing. As sensing technology, the magnetoresistive effects are promising candidates. A wide variety of anticipated sensing technologies have been already reviewed by Freitas *et al* [31], Tamanaha *et al* [217] and Wang and Li [218]. One of the first demonstrations that the GMR can be utilized for the detection of MNPs was discussed by Baselt *et al* [219]. This concept was used to demonstrate single MNP positioning and detection later on by Graham *et al* [220], and a comparison of Schotter *et al* [221] with fluorescent labels demonstrated the potential of magnetoresistive sensors in biotechnology. The PHE as sensing technology was discussed in 2004 and 2005 by Ejsing *et al* [91, 145]. This research opened the way for the wide use of NiFe/IrMn structure as a planar Hall sensor, especially for biological applications. To combine the high sensitivity and the high area of detection, Tu, *et al* developed an array of 24 planar Hall sensors, each sensor has a size of  $w \times w = 9 \mu\text{m}^2$  based on NiFe (20 nm)/IrMn (10 nm) bilayer structure. The sensors in the middle of the array showed a sensitivity of  $2.5 \text{ m}\Omega \text{ Oe}^{-1}$  and the sensor at the edge showed a sensitivity of  $2.3 \text{ m}\Omega \text{ Oe}^{-1}$ . These sensitivities allow the sensors to detect a single micromagnetic bead with a signal significantly higher compared to the signals of the micro magnetic beads in that period [148]. Although magnetic beads can be detected by placing them directly on the top of the sensor. The development of on-chip magnetic biosensors that provide easily repeatable results, may require the use of microfluidic systems. In order to compare the performance of the bridge and the cross planar Hall sensors for biological applications, Dalslet *et al* measured the Browning relaxation of magnetic nanobeads using both sensors [209]. The study showed that the signals measured by the bridge sensor are six times higher than those measured by the cross sensor.

**Table 2.** Illustration of the numerical value of sensitivity for the most common structures for planar Hall effect-based sensors.

Sensor architecture	Sensor structure	Sensitivity	Authors	Reference
Cross $3 \times 3 \mu\text{m}^2$	bilayer NiFe(20 nm)/IrMn(10 nm)	25 V/AT	Tu <i>et al</i>	[148]
Cross $5 \times 5 \mu\text{m}^2$	Trilayer NiFe(10)/Pt(0.8)/IrMn(8 nm)	38 V/AT	Pişkin <i>et al</i>	[162]
Cross $20 \times 20 \mu\text{m}^2$	Bilayer NiFe (30 nm)/IrMn(20 nm)	49.4 V/AT	Dalslet <i>et al</i>	[209]
Tilted cross-junction $5 \times 5 \mu\text{m}^2$	Trilayer NiFe(10 nm)/Pt(0.8 nm)/IrMn(8 nm)	58 V/AT	Pişkin <i>et al</i>	[162]
Cross $3 \times 3 \mu\text{m}^2$	Spin valve NiFe(16 nm)/Cu(1.2 nm)/NiFe(2 nm)/IrMn(15 nm)	72 V/AT	Hung <i>et al</i>	[174]
Tilted cross-junction $100 \times 50 \mu\text{m}^2$	Spin valve NiFe(6 nm)/Cu(3 nm)/NiFe(3 nm)/IrMn(15 nm)	95 V/AT	Hung <i>et al</i>	[189]
Cross $50 \times 50 \mu\text{m}^2$	Spin valve NiFe(16 nm)/Cu(1.2 nm)/NiFe(2 nm)/IrMn(15 nm)	76.15 V/AT	Hung <i>et al</i>	[178]
Cross $50 \times 50 \mu\text{m}^2$	Trilayer NiFe(10 nm)/Cu(0.2 nm)/NiFe(10 nm)	120 V/AT	Hung <i>et al</i>	[93, 112]
Cross $50 \times 50 \mu\text{m}^2$	Trilayer NiFe(10 nm)/Au(0.6 nm)/IrMn(10 nm)	236 V/AT	Li <i>et al</i>	[65]
dPHEB (bridge) $n = 1$ arms $l = 250$ (length) $\mu\text{m}$ , $w = 25 \mu\text{m}$	Bilayer NiFe(30 nm)/IrMn(20 nm)	181 V/AT	Østerberg <i>et al</i>	[200]
dPHEB (bridge) $n = 2$ arms $l = 250$ (length) $\mu\text{m}$ , $w = 25 \mu\text{m}$	Bilayer NiFe(30 nm)/IrMn(20 nm)	369 V/AT	Østerberg <i>et al</i>	[200]
dPHEB $n = 3$ arms $l = 250$ (length) $\mu\text{m}$ , $w = 25 \mu\text{m}$	Bilayer NiFe(30 nm)/IrMn(20 nm)	555 V/AT	Østerberg <i>et al</i>	[200]
Ring $n = 1$ (radius = 150 $\mu\text{m}$ , width $w = 5 \mu\text{m}$ )	Trilayer NiFe(10 nm)/Pt(0.8 nm)/IrMn(8 nm)	960 V/AT	Pişkin <i>et al</i>	[162]
Ring $n = 5$ (radius = 150 $\mu\text{m}$ , width $w = 5 \mu\text{m}$ )	Trilayer NiFe(10 nm)/Pt(0.8 nm)/IrMn(8 nm)	2990 V/AT	Pişkin <i>et al</i>	[162]
Multi bridge (mPHEB) $n = 3$ $w = 30 \mu\text{m}$ , $l = 600 \mu\text{m}$	bilayer NiFe (30 nm)/IrMn (20 nm)	1757	Henriksen <i>et al</i>	[193]
Multi bridge (mPHEB) $n = 5$ $w = 30 \mu\text{m}$ , $l = 600 \mu\text{m}$	bilayer NiFe (30 nm)/IrMn (20 nm)	2825	Henriksen <i>et al</i>	[193]
Multi bridge (mPHEB) $n = 7$ $w = 30 \mu\text{m}$ , $l = 600 \mu\text{m}$	bilayer NiFe (30 nm)/IrMn (20 nm)	3790 V/(AT)	Henriksen <i>et al</i>	[193]
Ring $n = 7$ $w = 5 \mu\text{m}$ $r = 120 \mu\text{m}$ . (the outer radius)	Trilayer NiFe(10)/Cu(0.2)/NiFe(10 nm) trilayer	6350 V/(AT)	Hung <i>et al</i>	[197]
Ring $n = 5$ $w = 5 \mu\text{m}$ $r = 120 \mu\text{m}$ . (the outer radius)	Trilayer NiFe(10 nm)/Cu(0.1 nm)/IrMn(10 nm)	12000 V/AT	Hung <i>et al</i>	[196]

Also, the bridge sensors were used in this study to measure the Browning relaxation of nano beads that were hybridized with DNA coil, and the obtained measurements are similar to those found when using a commercial AC susceptometer. The influence of temperature effects and the possibility of exchange biasing have been evaluated by Damsgaard *et al* [43, 151]. The compensation of parasitic magnetic fields by compensation layers was demonstrated by Dalslet *et al* [222]. The effect of the sensor's dimensions, stack, and the applied current on the self-heating of the sensor has been studied by Henriksen *et al* [198]. However, to our knowledge, no

study has considered the effect of self-heating on the magnetic state of the beads. Based on these improvements and optimizations on the planar Hall sensor, several papers have been published on the biological uses of such sensors, such as the detection of point mutations in DNA [223], the investigation of DNA denaturation under the effect of temperature or salt [224, 225], and the detection of DNA formed by the rolling circle amplification from a *Vibrio cholerae* DNA target and from a *Bacillus globigii* bacterial spore target [226]. Recently, PHE sensors have been integrated on flexible substrates, and a sensitivity better than 200 nT was shown by

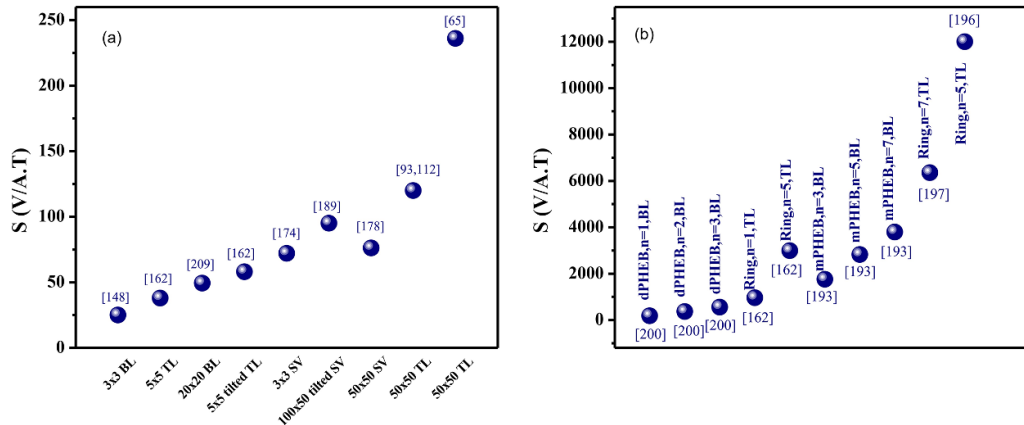


**Figure 11.** The graphical illustration of the varied sensitivity magnitudes with the junction geometry. (a) the sensitivity of the cross junction where SV, BL, and TL stand for spin valve, bilayer, and trilayer respectively attributed to their references, and (b) The bridge configuration junction sensitivities.

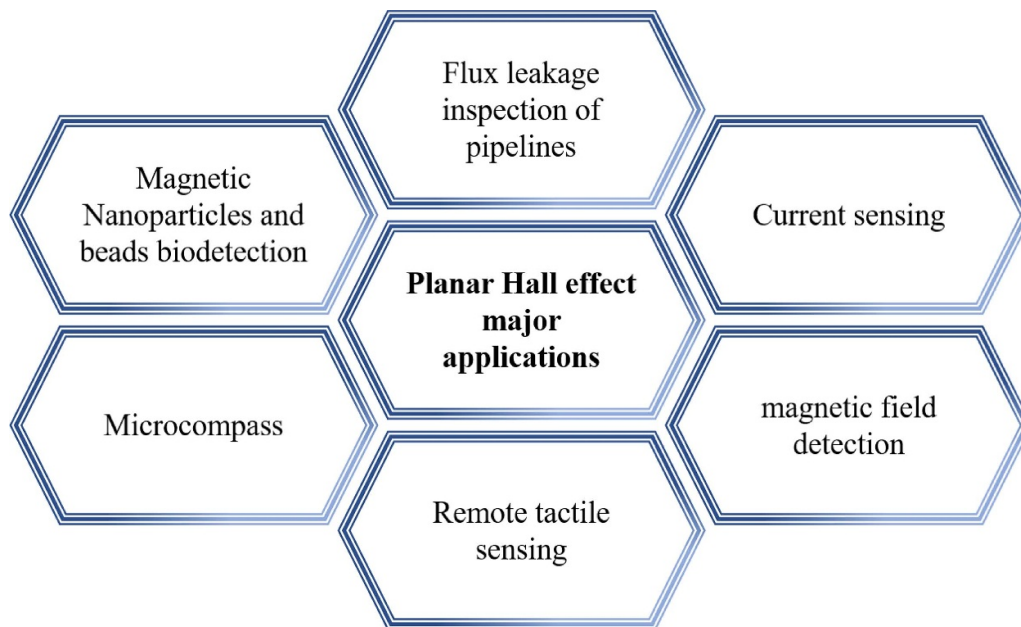


**Figure 12.** Major areas of application for the planar Hall effect-based sensors.

Granell *et al* [47], which is critically important for wearable devices or other such sensors otherwise attached to the body.

In addition to the detection of biomaterials [227–232], the use of PHE based sensors have been investigated in various application areas, such as magnetic micro/nano-sized particle detection/characterization [233–240], current sensing [241], very low magnetic field detection [53, 129, 242, 243], micro-electronic compasses [57, 244], remote tactile sensing [140], and flux leakage inspection of pipelines [44]. Several studies on flexible sensorics also show that flexible PHE sensors can be used in these application areas. These major application areas for PHE-based sensors are presented in figure 12. In the following section, we briefly discuss the MNP detection capability of the PHE sensor with a new technique which can be integrated with a microfluidic channel. Furthermore, the frontier studies of flexible PHE sensors will be addressed.

### 7.1. PHE sensors for MNPs detection integrated with microfluidic channels

The planar Hall sensor integrated into a microfluidic system was used to inspect the capturing of micromagnetic beads on the sensor [245, 246], and to measure the Brownian relaxation of nanomagnetic beads at room temperature [247, 248]. In previous studies, the magnetic beads are magnetized by the electromagnetic field created from the bias current that passes through the sensor. The advantage of this technique is that the magnetic field created from the beads has the same sign wherever the magnetic bead is located [249]. Therefore, the application of a high current inside the sensor increases the magnetic field created by the bead on the active area of the sensor. However, a high applied current can breakdown the sensor or even change the magnetic state of the magnetic bead or the magnetic particles. In contrast to

the self-field technique, when an external magnetic field is applied on the magnetic beads, the magnetic field created from beads located outside the sensor has an opposite sign to the magnetic field created by the beads inside the sensor [250], which reduces the total magnetic field created on the sensor.

Here, a new technique is briefly discussed, that was recently developed within an EU H2020 project (MADIA [251]). There MNPs are transported close to the sensors by the microfluidics. Then, in order to avoid external magnetic fields, they are magnetized by the sense current's magnetic field  $\vec{H}_{Oe}$  and the stray field of the MNPs is detected by the sensor. As discussed in [31], there are different types of sensors, that can be used for this purpose such as GMR-, TMR- or PHE-sensors that consist of a multilayered thin film stack with magnetic reference and other layers. Because the sensors are located in fluidics, they must be protected by a passivation layer deposited after lithography.

These sensors need to pick up the dipolar stray fields  $\vec{H}_S$  of the MNPs, which depend strongly on the magnetic moment of the MNP and the distance between MNP and sensor. Figure 13 shows the calculated strength of  $\vec{H}_S$  of a typical MNP as a function of this distance. It is obvious, that the sensors must be able to detect magnetic fields down to some mOe ( $10^{-7}$  T), and that the passivation layer between the sensor and the microfluidics should be as thin as possible. The red line indicates the cut-off for a 100 nm thick passivation layer

The most important test for evaluating the potential of different sensor types is, therefore, to measure the sensor response down to  $\approx 0.1$  mOe. To exploit the full sensitivity, an AC-measurement technique is used: There, the current through the sensor is driven at a frequency  $f$ . Simultaneously, the magnetic field is also applied with the same frequency and phase. Then, the resistance of the sense layer will change with the frequency  $f$ , too. This gives rise to a second harmonic component (frequency  $2f$ ) of the GMR, TMR and PHE-sensor signal. The basic idea behind this is to magnetize the MNPs directly by the Oersted-field created by the sense current. The major advantage behind this scheme is that the  $2f$ -component arises only, if magnetic material is above the sensor.

Figure 14, shows the first and second harmonic response of a PHE sensor operated in this mode to an external DC-field. The sense layer in this example is 10 nm Permalloy, that is weakly RKKY-coupled by 1.8 nm of Ru to a strongly exchange biased Permalloy layer. The  $2f$ -signal in this example saturates at  $\pm 10$  Oe and is slightly shifted to a positive external field by the weak RKKY-coupling. Thus, this coupling has two major advantages: first, it suppresses domain formation in the sense layer, and, second, at zero external field the response is close to linear. It shall be mentioned that a DC sensitivity of  $10 \mu\text{V Oe}^{-1}$  has been reached. The  $1f$  signal (left axis in figure 14) shows a signal change of about  $20 \mu\text{V Oe}^{-1}$  in zero field.

The potential to detect fields down to 1 mOe is demonstrated in figure 15, where the results of the sensitivity tests

for an exchange biased PHE sensor with a stack sequence  $\text{Ru}^{5\text{ nm}}/\text{Mn-Ir}^{10\text{ nm}}/\text{Ni-Fe}^{4\text{ nm}}/\text{Ru}^{1.8\text{ nm}}/\text{Ni-Fe}^{10\text{ nm}}/\text{Ta}^{2\text{ nm}}$  are shown.

Figure 15 demonstrates the potential of the PHE-sensors to detect small fields down to the range of mOe. Similar results have been obtained for the sensitivity of TMR- and GMR-sensors (not shown).

In addition to mOe sensitivity of the sensor, a magnetic field of some tens of Oersteds is needed to be generated to partially magnetize the MNPs in a microfluidic channel. On the other hand, this external magnetic field must NOT saturate the sensor, because then the detection of the mOe stray fields of the MNPs would be impossible. One approach is to use a single or a pair of highly conducting layers, which upon current loading would generate a magnetic field. This, however, requires additional insulating layers, making the lithographic process complicated and decreasing the yield of working sensor systems. In contrast to TMR-sensors, it is generally possible to use the sensor layers themselves as a field line. In figure 16, we show the calculated magnetic field as a function of the distance to the sensor surface for a typical sensor layout.

It becomes clear, that within a distance that is comparable to the wire width, the field decays only weakly with increasing distance and has amplitudes of some 10 Oe. Taking this into account, the PHE sensor is most probably the best choice. The stray field of the sense current is enough to produce a 1% magnetization in the MNPs that in turn leads to a stray field of some 10 mOe at distances of some  $\mu\text{m}$  from the MNP's center. Thus, the scheme to use the sense current itself for magnetizing the MNPs and then apply the  $2f$ -Lock-in technique for detection is based on a realistic scenario for sensing MNPs within microfluidics.

An additional critical issue is the passivation layer that must protect the sensors against the fluids in the microfluidic channels. The passivation layer must be free of pinholes and as thin as possible to minimize the distance between the sensor and the MNP (see figure 13). This surface chemistry must be compatible with the requirements for the bonding to the microfluidic channels. For reactively sputtered  $\text{TaO}_x$  or  $\text{Al}_2\text{O}_3$  at least about 200 nm thickness is necessary to protect in particular the edges of the sensor.  $\text{Al}_2\text{O}_3$  layers deposited by atomic layer deposition (ALD) are more promising for protection. There, a  $\text{Al}(\text{CH}_3)_3$ -precursor and  $\text{H}_2\text{O}$  gas are let into a reaction chamber in alternating cycles. The precursors can reach all surfaces of a sample and thus can cover edges by a homogeneous  $\text{Al}_2\text{O}_3$  layer. To evaluate the reliability of the ALD grown passivation layers, stressing by voltage ramping (0 V–10 V) and constant voltage (between 0 V and 10 V) was applied for thicknesses between 5 nm and 50 nm. An  $\text{Al}_2\text{O}_3$  layer of 20 nm thickness deposited by ALD turned out to provide a reliable protection of the sensors, which is by a factor of 10 thinner than sputter-deposited protections.

For real-world sensor operation, the magnetic field created by the sense current ( $\vec{H}_{Oe}$ ) has to be taken into account. In the case of a multilayer system, the net torque acting on the sense layer's magnetization depends on its position in the stack

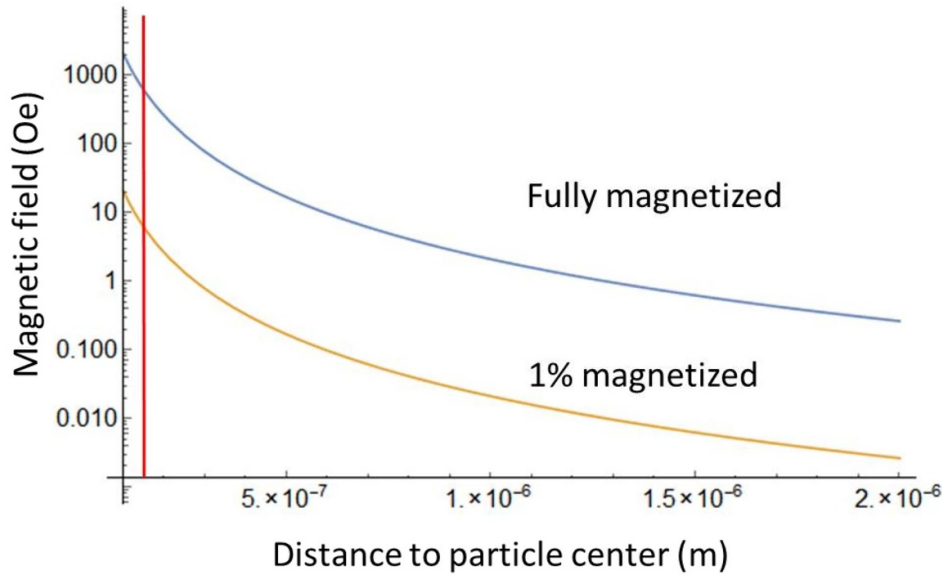


**Figure 13.** The magnetic stray field of a MNP with saturation magnetization of  $500 \text{ kA m}^{-1}$  and a diameter of 20 nm as a function of the distance from the particle’s center for full magnetization and for 1% of the saturation magnetization.

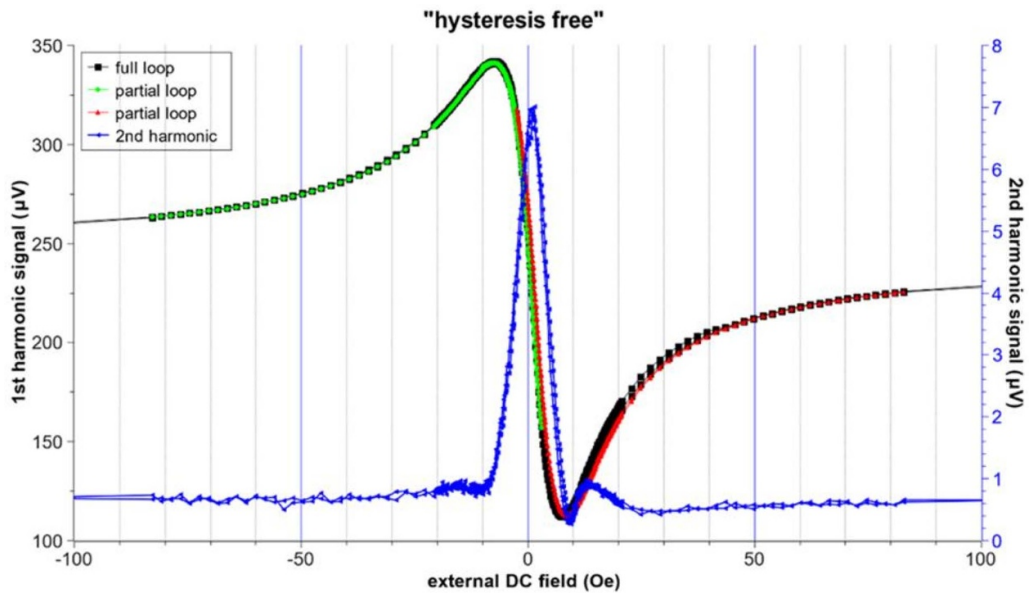


**Figure 14.** Hysteresis loop in first and second harmonic lock-in detection ( $\text{Ru}^{5 \text{ nm}}/\text{Mn-Ir}^{10 \text{ nm}}/\text{Ni-Fe}^{4 \text{ nm}}/\text{Ru}^{1.8 \text{ nm}}/\text{Ni-Fe}^{10 \text{ nm}}/\text{Ta}^{2 \text{ nm}}$  PHE stack) in second harmonic mode. The sense layer FM of the stack is marked in bold.

and on the thicknesses and the electrical conductivities of all layers involved. The influence of the Oersted field in asymmetric PHE stacks on the signal is shown in figure 17. The Oersted field of a DC sensor current of  $\pm 20 \text{ mA}$  shifts the sensor response by  $\pm 2.5 \text{ Oe}$  in this particular case.

If one uses an AC sensor current, the resulting  $\vec{H}_{\text{Oe}}$  will be an AC field, accordingly. For a quantitative evaluation of the ac  $1f$ - and  $2f$ -sensor signal, one needs to understand all contributions to the  $1f$  and  $2f$  components: As is known, the PHE is intimately related to the AMR. If  $\rho_{\parallel}$  is the longitudinal resistivity of a FM material for parallel (orthogonal) alignment of its magnetization and the current, one can define the AMR amplitude as  $(\rho_{\parallel} - \rho_{\perp})$ . The sensor current is taken as

an AC current in  $x$ -direction:  $I_x = I_0 \sin \omega t$ . Furthermore, the normalized hysteresis loop of the PHE sensor as a function of an external DC magnetic field in  $y$ -direction is described by  $f(H_y^{\text{DC}})$ . The AC sensor current is then directly connected to an AC Oersted field in  $y$ -direction:  $H_y^{\text{Oe}} = \gamma_y^{\text{Oe}} I_0 \sin \omega t$ , where  $\gamma_y^{\text{Oe}}$  is a constant depending on the effective asymmetry of the stack. As the sensor current generates  $\vec{H}_{\text{Oe}}$  for partially magnetizing the MNPs and as the stray field of the MNPs will have the same time dependence as their magnetic moment, a similar ansatz can be made for the stray field of the MNPs seen by the sense layer:  $H_y^{\text{MNP}} = \gamma_y^{\text{MNP}} I_0 \sin \omega t$ , where  $\gamma_y^{\text{MNP}}$  is a proportionality factor depending on the susceptibility of

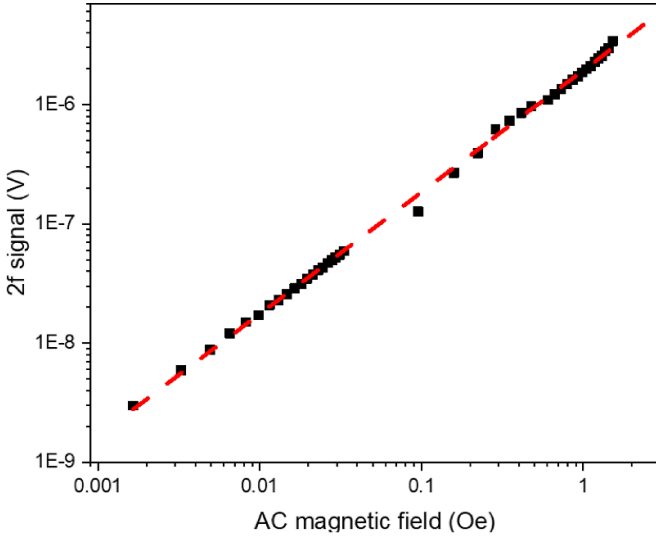


**Figure 15.** Sensitivity test of the  $2f$ -signal of a PHE sensor described in the text.

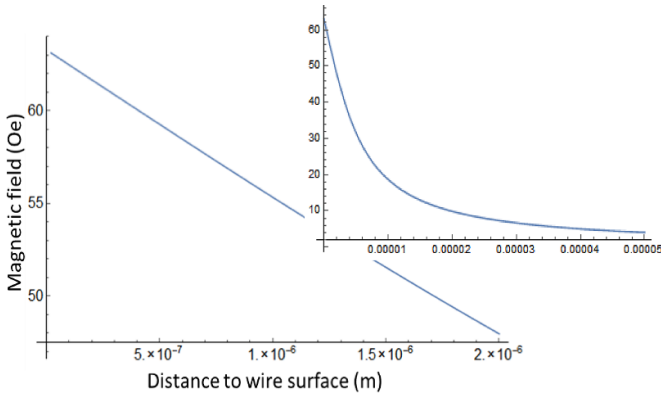


**Figure 16.** The magnetic field created by a 40 nm thick and 10  $\mu\text{m}$  wide wire at a current of 100 mA as a function of the distance to the wire surface. The inset shows the same up to a distance of 50  $\mu\text{m}$  (calculation by Biot–Savart’s law), where the  $1/\text{distance}$  dependence appears for distances larger than the wire width.

the MNPs and their lateral distribution in the vicinity of the sensor. Finally, a geometric factor  $\Omega_{\text{sensor}}$  takes into account the layer sequence, the sensor width and the total thickness of the sensor. Thus, the voltage analyzed by a lock-in amplifier with respect to the first and second harmonic term becomes:

$$\begin{aligned}
 V_y = & \Omega_{\text{sensor}} (\rho_{\parallel} - \rho_{\perp}) I_0 f(H_y^{\text{DC}}) \sin \omega t \\
 & + \Omega_{\text{sensor}} (\rho_{\parallel} - \rho_{\perp}) I_0^2 \frac{\partial f(H_y^{\text{DC}})}{\partial H_y^{\text{DC}}} \Big|_{H_y^{\text{DC}}} \\
 & \times (\gamma_y^{\text{MNP}} + \gamma_y^{\text{Oe}}) \sin^2 \omega t.
 \end{aligned} \quad (12)$$

The first term is the first harmonic signal which will not change in the presence of MNPs and might be useful for controlling the temperature. The second term includes the signal of the MNPs. If  $\vec{H}_{\text{Oe}}$  is balanced ( $\gamma_y^{\text{Oe}} = 0$ ), the second harmonic signal consists of some constants and the proportionality factor of the MNPs in the vicinity of the sensor. This is the required direct signal that can be fed to data processing. A large advantage is, that this signal is equal to zero if no MNPs are present.

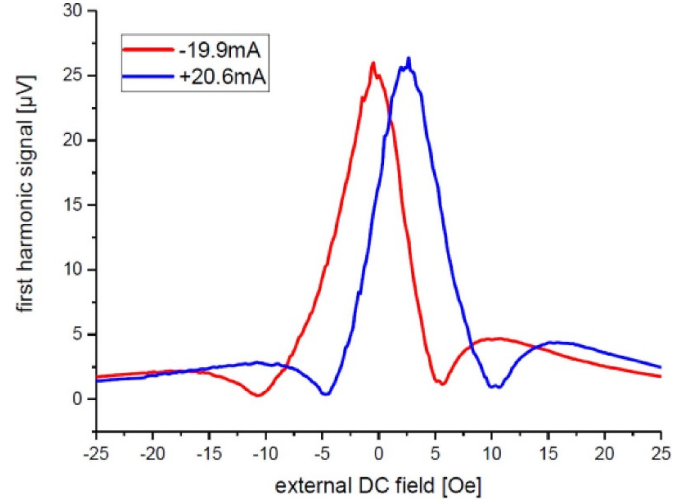


**Figure 17.** Derivative of hysteresis loops of a PHE sensor. The external DC field is applied in  $y$ -direction. As the current flow is in  $x$ -direction, the Oersted field must also be aligned in  $y$ -direction. We used DC currents of  $\pm 20$  mA in this case which results in a net Oersted field of about  $\pm 2.5$  Oe. The derivative has been taken by applying a small additional external AC field in  $y$ -direction and by taking the first harmonic lock-in signal.

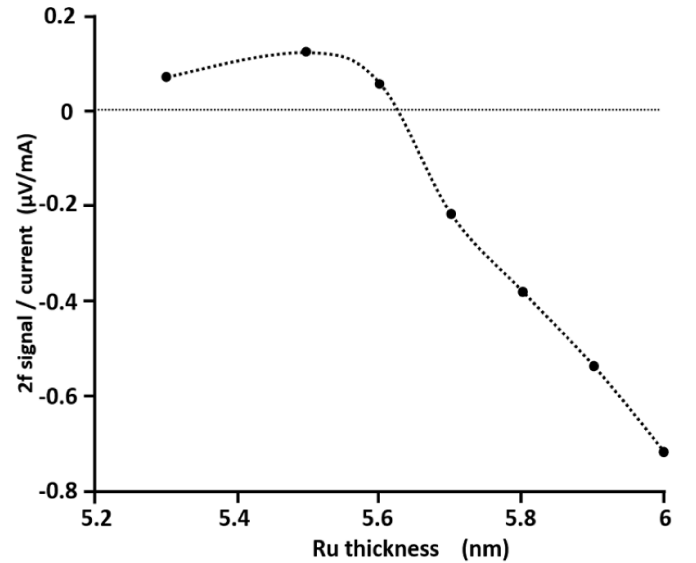


**Figure 18.** The measured second harmonic signal response of a PHE sensor normalized to the sense current as a function of the thickness of a Ru cap layer. The AC Oersted field in the sense layer is compensated at a Ru thickness between 5.6 nm and 5.7 nm. The dotted curve is a guide for the eye.

The compensation of the Oersted field can be obtained by varying the current distribution in the film stack. In figure 18, as an example the  $2f$ -signal of a PHE sensor stack is shown normalized to the sense current as a function of the thickness of a Ru-cover layer that is needed for contacting.

Thus, this example shows, that PHE-sensors fulfill the major requirements for detecting MNPs in microfluidics:

Within a Lock-in detection scheme, they can provide a thorough sensitivity and in the  $2f$ -component, they can be selective to magnetic entities close to the sensor if these entities are magnetized by  $\vec{H}_{0c}$ . In combination with a thin ALD passivation layer, this layout and measurement technique provides optimum conditions for further developing magnetic LOC systems for biotechnology.

## 7.2. Flexible sensorics based on PHE

Healthcare is a vital area for consideration with new and more powerful types of sensors [252–257]. The integration of PHE-based sensors with wearable devices has increased in recent years. A flexible MR device referring to the PHE was constructed by Oh *et al* [51] using a hybrid process of embedding an Ag nanoparticle electrode with thermal imprinting and magnetic multilayer sensor through sputtering on polyethylene naphthalate substrate. The comparison of the root mean square (RMS) and magnetic properties showed that exchange bias was reduced with the rise in roughness, and that the temperature holds no noteworthy impact on sensor performance. The Ag NP-paste was stable up to  $\theta \approx 90^\circ$  during convex bending while the Au electrode was stable up to  $\theta \approx 45^\circ$  only. Yet, sensor sensitivity was decreased due to the position of the sensor at the center during bending. The field sensitivity decrement is due to induced stress which increases linearly with the bending up to  $\theta = 45^\circ$ . Overall, the strain at the sensor position disturbs the field sensitivity of the MR signal that makes it essential to calibrate the signal when subjecting the sensor to static stress. Oh *et al* [50], developed a point-of-care analytic system to spot pathogenic bacteria. The system comprises a PHE sensor in conjunction with a magnetic bead coated by a specific antibody to a bacterial antigen. The sensor with Teflon passivation layer was fabricated over an organic substrate for conferring both flexibility and low-cost. Bacteria thus bound to the magnetic bead was readily distinguished with this sensor with no preceding preparatory steps. The response was measured for *Magneto-spirillum magneticum* AMB-1 at a minimum concentration of  $1.3 \times 10^8$  cells  $\text{ml}^{-1}$ . Furthermore, *Escherichia coli* was captured by immobilized anti-*E. coli* antibodies on the surface of the sensor and detected using magnetic bead labelled with anti-*E. coli* antibody. The detection limit of *E. coli* was found to be  $1.2 \times 10^3$  cells  $\text{ml}^{-1}$ . The design of a new temperature sensor able to detect body temperature by encompassing a magnetic sensor polymer relying on the PHE and a growing polymer was presented by Jeong *et al* [258]. Reliable repeatability, increased sensitivity and precision, and free thermal hysteresis, were demonstrated specifications for the proposed sensor. A differential planar Hall resistive (PHR) sensor was employed for the high precision open-type current sensor. The current sensor was designed to quantify a 1 A current, and nonlinearity of current  $\pm 0.5\%$ , as an example of a single-chip current sensor using the PHE sensor [45]. With a bioinspired robotic hand designed for tactile sensing, the system mimicked the natural joints of three fingers with both high sensitivity and the capability of grasping diverse items [259]. The application of the PHE for the angle orientation and distance sensors of

low fields triggered by magnetic objects was also developed in which a 20 nT limit of detection and high bendability was demonstrated confirmed [47]. The introduction of stable sensitivity through repeatable bending cycles of the PHE sensors was demonstrated. The subjected sensor is very sensitive to stress and strain fluctuations while sensitivity was maintained, thus showing the potential of such sensors for tactile sensing [52]. The bending consequences on the performance of the PHR sensors were considered, in which deformation has a reversible/irreversible threshold point depending on the substrate composition, thus paving the way to applications in medical diagnostics and wearable electronics [141].

## 8. Conclusion and perspectives

In this review, we have highlighted the most significant research on PHE sensors and their major potential applications. These results can be categorized into four basic sections: firstly, the origin of the AMR effect and theoretical background of PHE and magnetoresistive sensors. Secondly, dissimilar structures, such as simple Permalloy thin film, exchange biased structures (bilayers, trilayers) or spin-valve structures and their implications on the sensor sensitivity, field behavior, and stability. Thirdly, the effects of the sensor geometry on PHE sensitivity, and finally, the integration of these sensors into microfluidics and wearable devices. Micromagnetic simulations that describe the AMR, GMR and PHE in magnetic thin films were presented in order to have a better understanding of the presented data and sensors behavior at very low fields. Besides the aforementioned sections, a demonstration of the basic milestones for the evolution of PHE is displayed. Sensitivity comparison for various structures and junctions was introduced. Sensitivities between 25 V/AT for cross junctions to 12000 V/AT for structures with special sensor geometry such as ring shaped PHR were reported in this paper. It should be mentioned that the advantages of these sensors include higher sensitivity, lower detection limits, lower noise, with consequent increased S/N; hence, the consequences of junction aspect ratio, noise at different frequencies, and thermal stability were presented and discussed. Even though many groups worldwide have investigated these PHE sensors from different points of view, there are still some limitations regarding field sensitivity compared with GMR and TMR sensors. Further studies on new materials with better thermal stability and innovative junction geometries should be considered in order to improve the field sensitivity and to lower the detection limit. The reduction of noise with its different sources in the composed construction of the sensor was discussed. For example, when NiFeCr material was used instead of a Ta capping layer, decreased Barkhausen noise was observed with a S/N ratio increase of 50%. Operation at a wider temperature range is desirable for sensing applications. By careful microfabrication of NiFe/Cu/IrMn trilayer structures, an extremely low variation of a sensitivity of about  $4.5 \times 10^{-3}$  V/A/T/K for an extensive temperature span of  $-163^\circ\text{C}$  to  $86^\circ\text{C}$  was reported. However, better sensitivities are offered by other NM spacer layers such as Au,  $\text{Al}_2\text{O}_3$

deposited by ALD offers better passivation for practical bioapplications. Currently, no reports highlight the consequence of the self-heating on the magnetic state of the beads. For commercial development, further studies are needed on the integration procedures considering the advantages and disadvantages for lower cost and increased feasibility of the prototype devices. All of these areas need to be completely surveyed and monitored for more reliable, faster, and less costly devices for the next generation magnetic sensing technologies.

### Data availability statement

All data that support the findings of this study are included within the article (and any supplementary files).

### Acknowledgments

Our thanks to Hayden Clement of Charleston, South Carolina, in the United States for reviewing this work for grammatical and syntactic errors. His help is appreciated.

### ORCID iDs

Amir Elzwawy  <https://orcid.org/0000-0003-2206-1616>  
 Hasan Pişkin  <https://orcid.org/0000-0001-9927-4930>  
 Numan Akdoğan  <https://orcid.org/0000-0001-8469-5919>  
 Marius Volmer  <https://orcid.org/0000-0002-1160-9650>  
 Günter Reiss  <https://orcid.org/0000-0002-0918-5940>

### References

- [1] Mekawy M M, Hassan R Y A, Ramnani P, Yu X and Mulchandani A 2018 Electrochemical detection of dihydronicotinamide adenine dinucleotide using Al<sub>2</sub>O<sub>3</sub>-GO nanocomposite modified electrode *Arab. J. Chem.* **11** 942–9
- [2] Abou Hammad A B, Elzwawy A, Mansour A M, Alam M M, Asiri A M, Karim M R, Rahman M M and El Nahrawy A M 2020 Detection of 3,4-diaminotoluene based on Sr<sub>0.3</sub>Pb<sub>0.7</sub>TiO<sub>3</sub>/CoFe<sub>2</sub>O<sub>4</sub> core/shell nanocomposite via an electrochemical approach *New J. Chem.* **44** 7941–53
- [3] Alam M K, Rahman M M, Elzwawy A, Torati S R, Islam M S, Todo M, Asiri A M, Kim D and Kim C G 2017 Highly sensitive and selective detection of Bis-phenol A based on hydroxyapatite decorated reduced graphene oxide nanocomposites *Electrochim. Acta* **241** 353–61
- [4] Alam M K, Rahman M M, Abbas M, Torati S R, Asiri A M, Kim D and Kim C 2017 Ultra-sensitive 2-nitrophenol detection based on reduced graphene oxide/ZnO nanocomposites *J. Electroanal. Chem.* **788** 66–73
- [5] Salih E, Mekawy M, Hassan R Y A and El-Sherbiny I M 2016 Synthesis, characterization and electrochemical-sensor applications of zinc oxide/graphene oxide nanocomposite *J. Nanostruct. Chem.* **6** 137–44
- [6] Sedki M, Hassan R Y A, Hefnawy A and El-Sherbiny I M 2017 Sensing of bacterial cell viability using nanostructured bioelectrochemical system: rGO-hyperbranched chitosan nanocomposite as a novel microbial sensor platform *Sens. Actuators B* **252** 191–200
- [7] Yang X and Cheng H 2020 Recent developments of flexible and stretchable electrochemical biosensors *Micromachines* **11** 243
- [8] Jeerapan I and Poorahong S 2020 Review—flexible and stretchable electrochemical sensing systems: materials, energy sources, and integrations *J. Electrochem. Soc.* **167** 37573
- [9] Mani V, Beduk T, Khushaim W, Ceylan A E, Timur S, Wolfbeis O S and Salama K N 2021 Electrochemical sensors targeting salivary biomarkers: a comprehensive review *TrAC Trends Anal. Chem.* **135** 116164
- [10] Zhou X, Zhang Y, Yang J, Li J, Luo S and Wei D 2019 Flexible and highly sensitive pressure sensors based on microstructured carbon nanowalls electrodes *Nanomater* **9** 496
- [11] Sharma S, Chhetry A, Sharifuzzaman M, Yoon H and Park J Y 2020 Wearable capacitive pressure sensor based on MXene composite nanofibrous scaffolds for reliable human physiological signal acquisition *ACS Appl. Mater. Interfaces* **12** 22212–24
- [12] Jeong Y, Park J, Lee J, Kim K and Park I 2020 Ultrathin, biocompatible, and flexible pressure sensor with a wide pressure range and its biomedical application *ACS Sens.* **5** 481–9
- [13] Nguyen T, Dinh T, Phan H-P, Nguyen T-K, Md Faisal A R, Nguyen N-T and Dao D V 2020 Opto-electronic coupling in semiconductors: towards ultrasensitive pressure sensing *J. Mater. Chem. C* **8** 4713–21
- [14] Cui Z, Poblete F R and Zhu Y 2019 Tailoring the temperature coefficient of resistance of silver nanowire nanocomposites and their application as stretchable temperature sensors *ACS Appl. Mater. Interfaces* **11** 17836–42
- [15] Roriz P, Silva S, Frazão O and Novais S 2020 Optical fiber temperature sensors and their biomedical applications *Sensors* **20** 2113
- [16] Morsy M, Yahia I S, Zahran H Y, Meng F and Ibrahim M 2019 Portable and battery operated ammonia gas sensor based on CNTs/rGO/ZnO nanocomposite *J. Electron. Mater.* **48** 7328–35
- [17] Zhao Z-J, Ko J, Ahn J, Bok M, Gao M, Hwang S H, Kang H-J, Jeon S, Park I and Jeong J-H 2020 3D layer-by-layer Pdcontaining nanocomposite platforms for enhancing the performance of hydrogen sensors *ACS Sens.* **5** 2367–77
- [18] Morsy M, Ibrahim M, Yuan Z and Meng F 2020 Graphene foam decorated with ZnO as a humidity sensor *IEEE Sens. J.* **20** 1721–9
- [19] Jang J, Kang K, Raeis-Hosseini N, Ismukhanova A, Jeong H, Jung C, Kim B, Lee J-Y, Park I and Rho J 2020 Self-powered humidity sensor using chitosan-based plasmonic metal–hydrogel–metal filters *Adv. Opt. Mater.* **8** 1901932
- [20] Kapic A, Tsirova A, Verdini P G and Carrara S 2020 Humidity sensors for high energy physics applications: a review *IEEE Sens. J.* **20** 10335–44
- [21] Kuang K 2012 *Magnetic Sensors: Principles and Applications* (BoD—Books on Demand)
- [22] Ripka P and Závěta K 2009 Chapter three magnetic sensors: principles and applications *Handbook of Magnetic Materials* vol 18, ed K H J B T-H of M M Buschow (Amsterdam: Elsevier) pp 347–420 ([www.sciencedirect.com/science/article/pii/S1567271909018034](http://www.sciencedirect.com/science/article/pii/S1567271909018034))
- [23] Karsenty A 2020 A comprehensive review of integrated Hall effects in macro-, micro-, nanoscales, and quantum devices *Sensors* **20** 1–33

- [24] Ripka P, Arafat M M B T-R M in M S and M E 2019 *Magnetic Sensors: Principles and Applications* (Amsterdam: Elsevier)
- [25] Issadore D, Park Y I, Shao H, Min C, Lee K, Liong M, Weissleder R and Lee H 2014 Magnetic sensing technology for molecular analyses *Lab Chip* **14** 2385–97
- [26] Cao B, Wang K, Xu H, Qin Q, Yang J, Zheng W, Jin Q and Cui D 2020 Development of magnetic sensor technologies for point-of-care testing: fundamentals, methodologies and applications *Sens. Actuators A* **312** 112130
- [27] Murzin D, Mapps D J, Levada K, Belyaev V, Omelyanchik A, Panina L and Rodionova V 2020 Ultrasensitive magnetic field sensors for biomedical applications *Sensors* **20** 1569
- [28] Rizzi G, Lee J-R, Guldberg P, Dufva M, Wang S X and Hansen M F 2017 Denaturation strategies for detection of double stranded PCR products on GMR magnetic biosensor array *Biosens. Bioelectron.* **93** 155–60
- [29] Du W Y 2014 *Resistive, Capacitive, Inductive, and Magnetic Sensor Technologies* (Boca Raton, FL: CRC Press)
- [30] Su D, Wu K, Saha R, Peng C and Wang J-P 2019 Advances in magnetoresistive biosensors *Micromachines* **11** 34
- [31] Freitas P P, Ferreira R, Cardoso S and Cardoso F 2007 Magnetoresistive sensors *J. Phys.: Condens. Matter.* **19** 165221
- [32] Tumanski S 2001 *Thin Film Magnetoresistive Sensors* (Boca Raton, FL: CRC Press)
- [33] Pannetier M, Fermon C, Le Goff G, Simola J and Kerr E 2004 FemtoTesla magnetic field measurement with magnetoresistive sensors *Science* **304** 1648–50
- [34] Schotter J, Kamp P B, Becker A, Puhler A, Brinkmann D, Schepper W, Bruckl H and Reiss G 2002 A biochip based on magnetoresistive sensors *IEEE Trans. Magn.* **38** 3365–7
- [35] Denmark D J, Bustos-Perez X, Swain A, Phan M H, Mohapatra S and Mohapatra S S 2019 Readiness of magnetic nanobiosensors for point-of-care commercialization *J. Electron. Mater.* **48** 4749–61
- [36] Mehrotra P 2016 Biosensors and their applications—a review *J. Oral Biol. Craniofacial Res.* **6** 153–9
- [37] Hussein H A, Hassan R Y A, Chino M and Febbraio F 2020 Point-of-care diagnostics of COVID-19: from current work to future perspectives *Sensors* **20** 4289
- [38] Anon 2027 Permanent magnets market size & share Industry Report
- [39] Hirohata A, Yamada K, Nakatani Y, Prejbeanu L, Diény B, Pirro P and Hillebrands B 2020 Review on spintronics: principles and device applications *J. Magn. Magn. Mater.* **509** 166711
- [40] Primdahl F 1979 The fluxgate magnetometer *J. Phys. E* **12** 241–53
- [41] Nalwa H S 2002 *Handbook of Thin Film Materials* (New York: Academic)
- [42] Weiss R, Mattheis R and Reiss G 2013 Advanced giant magnetoresistance technology for measurement applications *Meas. Sci. Technol.* **24** 082001
- [43] Damsgaard C D, Freitas S C, Freitas P P and Hansen M F 2008 Exchange-biased planar Hall effect sensor optimized for biosensor applications *J. Appl. Phys.* **103** 07A302
- [44] Pham H Q, Tran B V, Doan D T, Le V S, Pham Q N, Kim K, Kim C, Terki F and Tran Q H 2018 Highly sensitive planar hall magnetoresistive sensor for magnetic flux leakage pipeline inspection *IEEE Trans. Magn.* **54** 1–5
- [45] Lee S, Hong S, Park W, Kim W, Lee J, Shin K, Kim C-G and Lee D 2018 High accuracy open-type current sensor with a differential planar hall resistive sensor *Sensors* **18** 2231
- [46] Bason Y, Klein L, Yau J B, Hong X, Hoffman J and Ahn C H 2006 Planar Hall-effect magnetic random access memory *J. Appl. Phys.* **99** 08R701
- [47] Granell P N, Wang G, Cañon Bermudez G S, Kosub T, Golmar F, Steren L, Fassbender J and Makarov D 2019 Highly compliant planar Hall effect sensor with sub 200 nT sensitivity *Npj Flex Electron.* **3** 3
- [48] Turner A P F 2013 Biosensors: sense and sensibility *Chem. Soc. Rev.* **42** 3184–96
- [49] Zhou W, JimmyHuang P J, Ding J and Liu J 2014 Aptamer-based biosensors for biomedical diagnostics *Analyst* **139** 2627–40
- [50] Oh S, Jadhav M, Lim J, Reddy V and Kim C 2013 An organic substrate based magnetoresistive sensor for rapid bacteria detection *Biosens. Bioelectron.* **41** 758–63
- [51] Oh S, Yu J, Lim J, Jadhav M, Lee T, Kim D and Kim C 2013 Highly flexible magnetoelectronic device integrated with embedded Ag nanoparticle electrode *IEEE Sens. J.* **13** 3957–61
- [52] Özer B, Pişkin H and Akdoğan N 2019 Shapeable planar hall sensor with a stable sensitivity under concave and convex bending *IEEE Sens. J.* **19** 5493–8
- [53] Quynh L K, Hien N T, Binh N H, Dung T T, Tu B D, Duc N H and Giang D T H 2019 Simple planar Hall effect based sensors for low-magnetic field detection *Adv. Nat. Sci. Nanosci. Nanotechnol.* **10** 025002
- [54] Anon Products and solutions for intelligent sensor technology Sensitec GmbH
- [55] Volmer M and Neamtu J 2010 Electrical and micromagnetic characterization of rotation sensors made from permalloy multilayered thin films *J. Magn. Magn. Mater.* **322** 1631–4
- [56] Volmer M and Neamtu J 2012 Optimisation of spin-valve planar Hall effect sensors for low field measurements *IEEE Trans. Magn.* **48** 1577–80
- [57] Montaigne F, Schuhl A, Van Dau F N and Encinas A 2000 Development of magnetoresistive sensors based on planar Hall effect for applications to microcompass *Sens. Actuators A* **81** 324–7
- [58] Sreevidya P V, Khan J, Barshilia H C, Ananda C M and Chowdhury P 2018 Development of two axes magnetometer for navigation applications *J. Magn. Magn. Mater.* **448** 298–302
- [59] Aceinna current sensors—aceinna: leader in MEMS sensor technology (<https://www.aceinna.com/current-sensors>)
- [60] Muşuroi C, Oproiu M, Volmer M and Firastrau I 2020 High sensitivity differential giant magnetoresistance (GMR) based sensor for non-contacting DC/AC current measurement *Sensors* **20** 323
- [61] Lin G, Makarov D and Schmidt O G 2017 Magnetic sensing platform technologies for biomedical applications *Lab Chip* **17** 1884–912
- [62] Volmer M and Avram M 2015 Using permalloy based planar hall effect sensors to capture and detect superparamagnetic beads for lab on a chip applications *J. Magn. Magn. Mater.* **381** 481–7
- [63] Gooneratne C P, Kodzius R, Li F, Foulds I G and Kosel J 2016 On-chip magnetic bead manipulation and detection using a magnetoresistive sensor-based micro-chip: design considerations and experimental characterization *Sensors* **16** 1369
- [64] Quang T, Young D, Parvatheeswara B and Kim C 2013 Novel planar Hall sensor for biomedical diagnosing lab-on-a-chip *State of the Art in Biosensors—General Aspects* (Rijeka: InTech)
- [65] Li X J, Feng C, Chen X, Zhang J Y, Liu Y W, Jiang S L, Liu Y, Li M H and Yu G H 2015 Enhanced planar hall sensitivity with better thermal stability by introducing interfacial modification of Au spacer *J. Magn. Magn. Mater.* **381** 386–9
- [66] Bagherzadeh R, Gorji M, Sorayani Bafgi M S and Saveh-Shemshaki N 2017 Electrospun conductive nanofibers for electronics *Woodhead Publishing Series in*

- Textiles* ed M B T-E N Afshari (Amsterdam: Woodhead Publishing) pp 467–519
- [67] Baibich M N, Broto J M, Fert A, Van Dau F N, Petroff F, Etienne P, Creuzet G, Friederich A and Chazelas J 1988 Giant magnetoresistance of (001)Fe/(001)Cr magnetic superlattices *Phys. Rev. Lett.* **61** 2472–5
- [68] Binasch G, Grünberg P, Saurenbach F and Zinn W 1989 Enhanced magnetoresistance in layered magnetic structures with antiferromagnetic interlayer exchange *Phys. Rev. B* **39** 4828–30
- [69] Prinz G A 1998 Magnetoelectronics *Science* **282** 1660–3
- [70] Yin Z, Bonizzoni E and Heidari H 2018 Magnetoresistive biosensors for on-chip detection and localization of paramagnetic particles *IEEE J. Electromagn. RF Microwaves Med. Biol.* **2** 179–85
- [71] Chang C-H, Dou K-P, Chen Y-C, Hong T-M and Kaun C-C 2015 Engineering the interlayer exchange coupling in magnetic trilayers *Sci. Rep.* **5** 16844
- [72] Grünberg P A 2001 Exchange anisotropy, interlayer exchange coupling and GMR in research and application *Sens. Actuators A* **91** 153–60
- [73] Meiklejohn W H and Bean C P 1956 New magnetic anisotropy *Phys. Rev.* **102** 1413–4
- [74] Nogués J and Schuller I K 1999 Exchange bias *J. Magn. Mater.* **192** 203–32
- [75] Vedmedenko E Y *et al* 2020 The 2020 magnetism roadmap *J. Phys. D: Appl. Phys.* **53** 453001
- [76] Moodera J S, Kinder L R, Wong T M and Meservey R 1995 Large magnetoresistance at room temperature in ferromagnetic thin film tunnel junctions *Phys. Rev. Lett.* **74** 3273–6
- [77] Vidal E G, Muñoz D R, Arias S I R, Moreno J S, Cardoso S, Ferreira R and Freitas P 2017 Electronic energy meter based on a tunnel magnetoresistive effect (TMR) current sensor *Materials* **10** 1134
- [78] Ribeiro P, Cardoso S, Bernardino A and Jamone L Highly sensitive bio-inspired sensor for fine surface exploration and characterization
- [79] Nishi Y and Magyari-Kope B 2019 *Advances in Non-volatile Memory and Storage Technology* (Cambridge: Woodhead Publishing)
- [80] Feng Y, Liu J, Klein T, Wu K and Wang J-P 2017 Localized detection of reversal nucleation generated by high moment magnetic nanoparticles using a large-area magnetic sensor *J. Appl. Phys.* **122** 123901
- [81] Thomson W 1857 XIX. On the electro-dynamic qualities of metals:—effects of magnetization on the electric conductivity of nickel and of iron *Proc. R. Soc. A* **8** 546–50
- [82] Tumanski S 2016 *Handbook of Magnetic Measurements* (Boca Raton, FL: CRC press)
- [83] West F G 1963 Rotating-field technique for galvanomagnetic measurements *J. Appl. Phys.* **34** 1171–3
- [84] McGuire T and Potter R 1975 Anisotropic magnetoresistance in ferromagnetic 3d alloys *IEEE Trans. Magn.* **11** 1018–38
- [85] Ky V D 1967 Theory of the anisotropy of resistance in ferromagnetic metals *Sov. Phys. JETP* **24** 995–9
- [86] Ruffer D, Huber R, Berberich P, Albert S, Russo-Averchi E, Heiss M, Arbiol J, Fontcuberta I M A and Grundler D 2012 Magnetic states of an individual Ni nanotube probed by anisotropic magnetoresistance *Nanoscale* **4** 4989–95
- [87] Stavroyiannis S 2003 Planar Hall effect and magnetoresistance in Ni<sub>81</sub>Fe<sub>19</sub> and Co square shaped thin films *Solid State Commun.* **125** 333–6
- [88] Zhao B, Yan X and Pakhomov A B 1997 Anisotropic magnetoresistance and planar Hall effect in magnetic metal-insulator composite films *J. Appl. Phys.* **81** 5527–9
- [89] Anon Low-cost, high-performance angular measurement
- [90] O'Handley R C 2003 Magnetic materials *Encyclopedia of Physical Science and Technology* ed R A B T-E of P S and Third E Meyers (Amsterdam: Elsevier) pp 919–44
- [91] Ejsing L, Hansen M F, Menon A K, Ferreira H A, Graham D L and Freitas P P 2005 Magnetic microbead detection using the planar Hall effect *J. Magn. Magn. Mater.* **293** 677–84
- [92] Li X J *et al* 2014 Large enhancement of planar Hall sensitivity in NiO/NiFe/NiO heterostructure by interfacial modification *Mater. Lett.* **126** 101–4
- [93] Hung T Q, Oh S, Sinha B, Jeong J-R, Kim D-Y and Kim C 2010 High field-sensitivity planar Hall sensor based on NiFe/Cu/IrMn trilayer structure *J. Appl. Phys.* **107** 09E715
- [94] Mahfoud M *et al* 2019 Reduced thermal dependence of the sensitivity of a planar Hall sensor *Appl. Phys. Lett.* **115** 072402
- [95] Antonov I, Vatskichev L and Vatskicheva M 1997 Planar Hall effect in thin magnetic films with domain structure *J. Magn. Magn. Mater.* **169** 25–30
- [96] Santos J A M, Kakazei G N, Pereira A M, Pogorelov Y G, Carpinteiro F S and Sousa J B 2001 Galvanomagnetic effects in Ni<sub>81</sub>Fe<sub>19</sub> thin films under in-plane and out-of-plane magnetic field *Mater. Sci. Forum* **373–376** 509–12
- [97] Kim H, Reddy V, Kim K W, Jeong I, Hu X H and Kim C G 2014 Single magnetic bead detection in a microfluidic chip using planar hall effect sensor *J. Magn.* **19** 10–14
- [98] Anon PC micromagnetics simulator release 2.0
- [99] Oh S J, Le T T, Kim G W and Kim C G 2007 Size effect on NiFe/Cu/NiFe/IrMn spin-valve structure for an array of PHR sensor element *Phys. Status Solidi Appl. Mater. Sci.* **204** 4075–8
- [100] Elzawawy A, Kim S, Talantsev A and Kim C 2019 Equisensitive adjustment of planar Hall effect sensor's operating field range by material and thickness variation of active layers *J. Phys. D: Appl. Phys.* **52** 285001
- [101] Ngan Luong T Q, Cao T A and Cao Dao T 2013 Low-concentration organic molecules detection via surface-enhanced Raman spectroscopy effect using Ag nanoparticles-coated silicon nanowire arrays *Adv. Nat. Sci. Nanosci. Nanotechnol.* **4** 015017
- [102] Épshtein É M 2002 Planar hall effect in ferromagnets *Phys. Solid State* **44** 1327–9
- [103] Jeon T, Lee J H, Talantsev A and Kim C G 2019 Planar Hall resistance sensor with improved thermal stability *IEEE Magn. Lett.* **10** 1–5
- [104] Hunte F 2004 *Determination of Exchange Anisotropy by ac-AMR and Planar Hall Effect* (Minneapolis: University of Minnesota)
- [105] Lee K J *et al* 2018 Magnetization reversal in trilayer structures consisting of GaMnAs layers with opposite signs of anisotropic magnetoresistance *Sci. Rep.* **8** 2288
- [106] Vig J R and Walls F L 2000 A review of sensor sensitivity and stability *Proceedings of the 2000 IEEE/EIA Int. Frequency Control Symp. and Exhibition (Cat. No.00CH37052)* pp 30–33
- [107] Scheinfein M R and Price E A 1997 LLG user manual v2. 50 code LLG simulator can be found (available at: <http://llgmicro.home.mindspring.com>)
- [108] Lim J, Sinha B, Ramulu T S, Kim K, Kim D-Y and Kim C 2013 NiCo sensing layer for enhanced signals in planar hall effect sensors *Met. Mater. Int.* **19** 875–8
- [109] Bason Y, Klein L, Yau J-B, Hong X and Ahn C H 2004 Giant planar Hall effect in colossal magnetoresistive La<sub>0.84</sub>Sr<sub>0.16</sub>MnO<sub>3</sub> thin films *Appl. Phys. Lett.* **84** 2593–5

- [110] Thanh N T, Kim K W, Kim C O, Shin K H and Kim C G 2007 Microbeads detection using planar Hall effect in spin-valve structure *J. Magn. Magn. Mater.* **316** e238–41
- [111] Won J, Shin J, Lee S, Lee H, Yoo T, Lee S, Liu X and Furdyna J K 2013 Planar Hall effect in a single GaMnAs film grown on Si substrate *J. Cryst. Growth* **378** 361–4
- [112] Hung T Q, Oh S, Anandakumar S, Jeong J R, Kim D Y and Kim C 2009 Optimization of the multilayer structures for a high field-sensitivity biochip sensor based on the planar Hall effect *IEEE Trans. Magn.* **45** 4518–21
- [113] Lu Z Q, Pan G, Lai W Y, Mapps D J and Clegg W W 2002 Exchange anisotropy in NiFe/FeMn bilayers studied by planar Hall effect *J. Magn. Magn. Mater.* **242–245** 525–8
- [114] Lu Z Q, Pan G and Lai W Y 2001 Planar Hall effect in NiFe/NiMn bilayers *J. Appl. Phys.* **90** 1414–8
- [115] Li G, Yang T, Hu Q and Lai W 2000 Exchange coupling in NiFe/NiMn films studied by pseudo-Hall effect *Appl. Phys. Lett.* **77** 1032–4
- [116] Kim D Y, Park B S and Kim C G 2000 Optimization of planar Hall resistance using biaxial currents in a NiO/NiFe bilayer: enhancement of magnetic field sensitivity *J. Appl. Phys.* **88** 3490–4
- [117] Nemoto A, Otani Y, Kim S G, Fukamichi K, Kitakami O and Shimada Y 1999 Magnetoresistance and planar Hall effects in submicron exchange-coupled NiO/Fe<sub>19</sub>Ni<sub>81</sub> wires *Appl. Phys. Lett.* **74** 4026–8
- [118] Chen Y-T 2008 The effect of interface texture on exchange biasing in Ni<sub>80</sub>Fe<sub>20</sub>/Ir<sub>20</sub>Mn<sub>80</sub>System *Nanoscale Res. Lett.* **4** 90
- [119] Anderson G, Huai Y and Miloslawsky L 2000 CoFe/IrMn exchange biased top, bottom, and dual spin valves *J. Appl. Phys.* **87** 6989–91
- [120] Ky V D 1968 Planar Hall effect in ferromagnetic films *Phys. Status Solidi* **26** 565–9
- [121] Goldberg C and Davis R E 1954 New galvanomagnetic effect *Phys. Rev.* **94** 1121–5
- [122] Yau K L and Chang J T H 1971 The planar Hall effect in thin foils of Ni-Fe alloy *J. Phys. F* **1** 38–43
- [123] Ky V D 1965 N IA 2-Dimension galvanomagnetic effect in thin ferromagnetic films *Ser. Fiz.* **29** 576
- [124] Ky V D 1967 Planar Hall and nernst effect in ferromagnetic metals *Phys. Status Solidi* **22** 729–36
- [125] Ky V D 1966 Plane Hall effect in ferromagnetic metals *Sov. Phys. JETP* **23** 809–13
- [126] Ky V D 1966 The nernst effect in permalloy films *Phys. Status Solidi* **17** K203–5
- [127] Vatskichev L, Mucha J, Georgiev Z and Vatskicheva M 1990 Measurements of the rotational hysteresis losses in magnetic films by the planar hall effect *Phys. Status Solidi* **118** K95–7
- [128] Berger L 1991 Galvanomagnetic voltages in the vicinity of a domain wall in ferromagnetic thin films *J. Appl. Phys.* **69** 1550–5
- [129] Schuhl A, Van Dau F N and Childress J R 1995 Low-field magnetic sensors based on the planar Hall effect *Appl. Phys. Lett.* **66** 2751–3
- [130] Schuhl A, Van Dau F N and Childress J R 1995 Nanotesla detection using the planar hall effect *Mater. Res. Soc. Symp. Proc.* **384** 15–20
- [131] Van Dau F N, Schuhl A, Childress J R and Sussiau M 1996 Magnetic sensors for nanotesla detection using planar Hall effect *Sens. Actuators A* **53** 256–60
- [132] Ogrin F Y, Lee S L and Ogrin Y F 2000 Investigation of perpendicular anisotropy of a thin film using the planar Hall effect *J. Magn. Magn. Mater.* **219** 331–9
- [133] Rizzi G 2014 Planar Hall effect sensors for biodetection Ph.D. Thesis Technical University of Denmark
- [134] Volmer M and Avram M 2013 Signal dependence on magnetic nanoparticles position over a planar Hall effect biosensor *Microelectron. Eng.* **108** 116–20
- [135] Ejsing L W 2006 *Planar Hall Sensor for Influenza Immunoassay* (Kongens Lyngby: MIC-Department of Micro and Nanotechnology, Technical University of Denmark)
- [136] Oh S, Anandakumar S, Lee C, Kim K W, Lim B and Kim C 2011 Analytes kinetics in lateral flow membrane analyzed by cTnI monitoring using magnetic method *Sens. Actuators B* **160** 747–52
- [137] Henriksen A D, Rizzi G and Hansen M F 2015 Experimental comparison of ring and diamond shaped planar Hall effect bridge magnetic field sensors *J. Appl. Phys.* **118** 103901
- [138] Lee S, Bac S-K, Choi S, Lee H, Yoo T, Lee S, Liu X, Dobrowolska M and Furdyna J K 2017 Non-volatile logic gates based on planar Hall effect in magnetic films with two in-plane easy axes *Sci. Rep.* **7** 1115
- [139] Elzawy A, Talantsev A and Kim C G 2018 Free and forced Barkhausen noises in magnetic thin film based cross-junctions *J. Magn. Magn. Mater.* **458** 292–300
- [140] Oh S, Jung Y, Kim S, Kim S, Hu X, Lim H and Kim C 2017 Remote tactile sensing system integrated with magnetic synapse *Sci. Rep.* **7** 16963
- [141] Kim M, Oh S, Jeong W, Talantsev A, Jeon T, Chaturvedi R, Lee S and Kim C 2020 Highly bendable planar Hall resistance sensor *IEEE Magn. Lett.* **11** 1–5
- [142] Ky V-D 1966 Plane hall effect in ferromagnetic metals *J. Exp. Theor. Phys.* **23** 809
- [143] Chang C-R 2000 A hysteresis model for planar Hall effect in thin films *IEEE Trans. Magn.* **36** 1214–7
- [144] Battarel C and Galinier M 1969 Optimization of the planar hall effect in ferromagnetic thin films for device design *IEEE Trans. Magn.* **5** 18–22
- [145] Ejsing L, Hansen M F, Menon A K, Ferreira H A, Graham D L and Freitas P P 2004 Planar hall effect sensor for magnetic micro- and nanobead detection *Appl. Phys. Lett.* **84** 4729–31
- [146] Roy A, Sampathkumar P and Anil Kumar P S 2020 Development of a very high sensitivity magnetic field sensor based on planar Hall effect *Measurement* **156** 107590
- [147] Nhalil H, Givon T, Das P T, Hasidim N, Mor V, Schultz M, Amrusi S, Klein L and Grosz A 2019 Planar Hall effect magnetometer with 5 pT resolution *IEEE Sens. Lett.* **3** 1–4
- [148] Tu B D, Hung T Q, Thanh N T, Danh T M, Duc N H and Kim C G 2008 Planar Hall bead array counter microchip with NiFe/IrMn bilayers *J. Appl. Phys.* **104** 1–5
- [149] Chui K M, Adeyeye A O and Li M H 2008 Effect of seed layer on the sensitivity of exchange biased planar Hall sensor *Sens. Actuators A* **141** 282–7
- [150] Qejvanaj F, Zubair M, Persson A, Mohseni S M, Fallahi V, Sani S R, Chung S, Le T, Magnusson F and Akerman J 2014 Thick double-biased IrMn/NiFe/IrMn planar hall effect bridge sensors *IEEE Trans. Magn.* **50** 4006104
- [151] Damsgaard C D, Dalslet B T, Freitas S C, Freitas P P and Hansen M F 2009 Temperature effects in exchange-biased planar hall sensors for bioapplications *Sens. Actuators A* **156** 103–8
- [152] Thanh N T, Chun M G, Ha N D, Kim K Y, Kim C O and Kim C G 2006 Thickness dependence of exchange anisotropy in NiFe/IrMn bilayers studied by planar Hall effect *J. Magn. Magn. Mater.* **305** 432–5
- [153] Thanh N T *et al* 2007 Thickness dependence of parallel and perpendicular anisotropic resistivity in Ta/NiFe/IrMn/Ta multilayer studied by anisotropic magnetoresistance and planar Hall effect *J. Appl. Phys.* **101** 53702

- [154] Kim D Y, Kim C G, Park B S and Park C M 2000 Thickness dependence of planar Hall resistance and field sensitivity in NiO(30 nm)/NiFe(t) bilayers *J. Magn. Magn. Mater.* **215** 585–8
- [155] Zhao Z D, Li M H, Kang P, Zhao C J, Zhang J Y, Zhou L J, Zhao Y C, Jiang S L and Yu G H 2015 The influence of ultrathin Cu interlayer in NiFe/IrMn interface on rotation of the magnetic moments *Appl. Surf. Sci.* **332** 710–5
- [156] Li X J, Feng C, Chen X, Liu Y, Liu Y W, Li M H and Yu G H 2014 Effects of interfacial roughness on the planar Hall effect in NiFe/Cu/IrMn multilayers *Appl. Phys. A* **118** 505–9
- [157] Morgunov R B, Talantsev A D, Bakhmet'ev M V and Granovskii N V 2020 Exchange interactions in NiFe/Ta/IrMn heterostructures under conditions of tantalum deficiency *Phys. Solid State* **62** 1033–8
- [158] Gökemeijer N J, Ambrose T and Chien C L 1997 Long-range exchange bias across a spacer layer *Phys. Rev. Lett.* **79** 4270–3
- [159] Yoo Y-G-G, Min S-G-G and Yu S-C-C 2006 Influence of spacer layer in exchange coupled NiFe/Cu/IrMn trilayer structure *J. Magn. Magn. Mater.* **304** e718–20
- [160] Thomas L, Kellock A J and Parkin S S P 2000 On the exchange biasing through a nonmagnetic spacer layer *J. Appl. Phys.* **87** 5061–3
- [161] Li K, Guo Z, Han G, Qiu J and Wu Y 2003 Abnormal temperature dependence of exchange bias in the NiFe<sub>5</sub>/Ta<sub>0.2</sub>/IrMn<sub>8</sub> system *J. Appl. Phys.* **93** 6614–6
- [162] Pişkin H and Akdoğan N 2019 Interface-induced enhancement of sensitivity in NiFe/Pt/IrMn-based planar hall sensors with nanoTesla resolution *Sens. Actuators A* **292** 24–29
- [163] Pişkin H 2020 Fabrication and Characterization of NiFe/X/IrMn (X: Cu, Cr, Pt)-Based Planar Hall Effect Sensors Ph.D Thesis (Gebze Technical University)
- [164] Pişkin H and Akdoğan N 2020 Tuning the magnetic field sensitivity of planar Hall effect sensors by using a Cr spacer layer in a NiFe/Cr/IrMn trilayer structure *Turk. J. Phys.* **44** 554–63
- [165] Demirci E 2020 Anisotropic magnetoresistance and planar Hall effect in magnetoresistive NiFe/Pt thin film *Turk. J. Phys.* **44** 77–84
- [166] Xu Y, Yang Y, Xie H and Wu Y 2019 Spin Hall magnetoresistance sensor using Au<sub>x</sub>Pt<sub>1-x</sub> as the spin-orbit torque biasing layer *Appl. Phys. Lett.* **115** 182406
- [167] Cho S, Baek S C, Lee K-D, Jo Y and Park B-G 2015 Large spin Hall magnetoresistance and its correlation to the spin-orbit torque in W/CoFeB/MgO structures *Sci. Rep.* **5** 14668
- [168] Nguyen M-H, Zhao M, Ralph D C and Buhrman R A 2016 Enhanced spin Hall torque efficiency in Pt<sub>100-x</sub>Al<sub>x</sub> and Pt<sub>100-x</sub>Hf<sub>x</sub> alloys arising from the intrinsic spin Hall effect *Appl. Phys. Lett.* **108** 242407
- [169] Zhu L, Zhu L, Shi S, Sui M, Ralph D C and Buhrman R A 2019 Enhancing spin-orbit torque by strong interfacial scattering from ultrathin insertion layers *Phys. Rev. Appl.* **11** 61004
- [170] Kim J, Sheng P, Takahashi S, Mitani S and Hayashi M 2016 Spin hall magnetoresistance in metallic bilayers *Phys. Rev. Lett.* **116** 97201
- [171] Talantsev A, Elzawawy A and Kim C 2018 Effect of NiFeCr seed and capping layers on exchange bias and planar Hall voltage response of NiFe/Au/IrMn trilayer structures *J. Appl. Phys.* **123** 173902
- [172] Henriksen A D, Rizzi G and Hansen M F 2016 Planar Hall effect bridge sensors with NiFe/Cu/IrMn stack optimized for self-field magnetic bead detection *J. Appl. Phys.* **119** 93910
- [173] Thanh N T, Parvatheeswara Rao B, Duc N H and Kim C 2007 Planar Hall resistance sensor for biochip application *Phys. Status Solidi Appl. Mater. Sci.* **204** 4053–7
- [174] Hung T Q, Oh S, Jeong J R and Kim C G 2010 Spin-valve planar Hall sensor for single bead detection *Sens. Actuators A* **157** 42–46
- [175] Jeong I, Eu Y J, Kim K W, Hu X H, Sinha B and Kim C G 2012 Magnetic sensor-based detection of picoliter volumes of magnetic nanoparticle droplets in a microfluidic chip *J. Magn.* **17** 302–7
- [176] Bui D T, Tran M D, Nguyen H D and Nguyen H B 2012 Influence of CoFe and NiFe pinned layers on sensitivity of planar Hall biosensors based on spin-valve structures *Adv. Nat. Sci. Nanosci. Nanotechnol.* **3** 045019
- [177] Neamtu J, Volmer M and Neamtu M C 2018 Spin-valve structures with anisotropic magneto-resistance (AMR) for planar Hall effect (PHE) sensing applications *Optoelectron. Adv. Mater. Commun.* **12** 603–7
- [178] Hung T Q, Oh S J, Tu B D, Duc N H, Phong L V, AnandaKumar S, Jeong J R and Kim C G 2009 Sensitivity dependence of the planar Hall effect sensor on the free layer of the spin-valve structure *IEEE Trans. Magn.* **45** 2374–7
- [179] Tu B D, Cuong L V, Hung T Q, Giang D T H, Danh T M, Duc N H and Kim C 2009 Optimization of spin-valve structure NiFe/Cu/NiFe/IrMn for planar hall effect based biochips *IEEE Trans. Magn.* **45** 2378–82
- [180] Wang S, Gao T, Wang C and He J 2013 Studies of anisotropic magnetoresistance and magnetic property of Ni<sub>81</sub>Fe<sub>19</sub>ultra-thin films with the lower base vacuum *J. Alloys Compd.* **554** 405–7
- [181] Lee W-Y, Toney M F, Tameerug P, Allen E and Mauri D 2000 High magnetoresistance permalloy films deposited on a thin NiFeCr or NiCr underlayer *J. Appl. Phys.* **87** 6992–4
- [182] Lee W Y, Toney M F and Mauri D 2000 High magnetoresistance in sputtered Permalloy thin films through growth on seed layers of (Ni<sub>0.81</sub>Fe<sub>0.19</sub>)<sub>1-x</sub>Cr<sub>x</sub> *IEEE Trans. Magn.* **36** 381–5
- [183] Sheng S, Li W, Li M and Yu G 2012 Investigation on interface of NiFeCr/NiFe/Ta films with high magnetic field sensitivity *Rare Met.* **31** 22–26
- [184] He J F and Wang S Y 2012 Effects of substrate temperature and buffer layer on the anisotropic magnetoresistance of Ni<sub>81</sub>Fe<sub>19</sub> ultra thin films *Optoelectron. Adv. Mater. Commun.* **6** 165–8
- [185] Elzawawy A A I 2019 Fabrication and optimization of magnetoresistive thin film structure for improved spintronic sensors *Doctoral dissertation* DGIST
- [186] Liu J, Duan C-K and Zheng R L 2005 Influence of seed layer NiFeNb on magnetic properties of nanometer permalloy films *Int. J. Mod. Phys. B* **19** 621–5
- [187] Wang S, Wang C, Gao Y, Gao T, Hu G and Zhang H 2013 Anisotropic magnetoresistance of Ni<sub>81</sub>Fe<sub>19</sub> films on NiFeNb buffer layer *J. Alloys Compd.* **575** 419–22
- [188] Kim C G, Park B S, Kim D Y, Song J S and Min B K 2001 Combined effects of MR and PHR Using biaxial currents in NiO/NiFe *Mater. Sci. Forum* **373–376** 365–8
- [189] Hung T Q, Jeong J-R, Kim D-Y, Duc N H and Kim C 2009 Hybrid planar Hall-magnetoresistance sensor based on tilted cross-junction *J. Phys. D: Appl. Phys.* **42** 55007
- [190] Donolato M, Dalslet B T, Damsgaard C D, Gunnarsson K, Jacobsen C S, Svedlindh P and Hansen M F 2011 Size-dependent effects in exchange-biased planar Hall effect sensor crosses *J. Phys. D: Appl. Phys.* **109** 064511
- [191] Li M, Zhao Z, Ma L, Yu G G, Lu X, Teng J, Yu G G, Zhou W, Amiri P K and Wang K L 2015 The influence of an MgO nanolayer on the planar Hall effect in NiFe films *J. Appl. Phys.* **117** 123908

- [192] Hung T Q, Rao B P and Kim C 2009 Planar Hall effect in biosensor with a tilted angle of the cross-junction *J. Magn. Mater.* **321** 3839–41
- [193] Henriksen A D, Dalslet B T, Skieller D H, Lee K H, Okkels F and Hansen M F 2010 Planar Hall effect bridge magnetic field sensors *Appl. Phys. Lett.* **97** 13507
- [194] Oh S, Patil P B, Hung T Q, Lim B, Takahashi M, Kim D Y and Kim C 2011 Hybrid AMR/PHR ring sensor *Solid State Commun.* **151** 1248–51
- [195] Persson A, Bejhed R S, Nguyen H, Gunnarsson K, Dalslet B T, Østerberg F W, Hansen M F and Svedlindh P 2011 Low-frequency noise in planar Hall effect bridge sensors *Sens. Actuators A* **171** 212–8
- [196] Hung T Q, Terki F, Kamara S, Kim K, Charar S and Kim C 2015 Planar Hall ring sensor for ultra-low magnetic moment sensing *J. Appl. Phys.* **117** 154505
- [197] Sinha B, Hung T Q, Ramulu T S, Oh S, Kim K, Kim D-Y, Terki F and Kim C 2013 Planar Hall resistance ring sensor based on NiFe/Cu/IrMn trilayer structure *J. Appl. Phys.* **113** 63903
- [198] Henriksen A D, Rizzi G, Østerberg F W and Hansen M F 2015 Optimization of magnetoresistive sensor current for on-chip magnetic bead detection using the sensor self-field *J. Magn. Mater.* **380** 209–14
- [199] Qejvanaj F, Mazraati H, Jiang S, Persson A, Sani S R, Chung S, Magnusson F and Åkerman J 2015 Planar hall-effect bridge sensor with NiFeX (X = Cu, Ag, and Au) sensing layer *IEEE Trans. Magn.* **51** 4005404
- [200] Østerberg F W, Rizzi G, Henriksen A D and Hansen M F 2014 Planar Hall effect bridge geometries optimized for magnetic bead detection *J. Appl. Phys.* **115** 184505
- [201] Sinha B, Oh S, Ramulu T S, Lim J, Kim D Y and Kim C G 2011 Planar hall effect ring sensors for high field-sensitivity *Adv. Mater. Res.* **317–319** 1136–40
- [202] Mor V, Schultz M, Sinwani O, Grosz A, Paperno E and Klein L 2012 Planar Hall effect sensors with shape-induced effective single domain behavior *J. Appl. Phys.* **111** 07E519
- [203] Hansen M F and Rizzi G 2017 Exchange-biased AMR bridges for magnetic field sensing and biosensing *IEEE Trans. Magn.* **53** 1–11
- [204] Jen S U, Lee J Y, Yao Y D and Chen W L 2001 Transverse field dependence of the planar Hall effect sensitivity in permalloy films *J. Appl. Phys.* **90** 6297–301
- [205] Hirohata A, Yao C C, Leung H T, Xu Y B, Guertler C M and Bland J A C 2000 Magnetic domain studies of permalloy wire-based structures with junctions *IEEE Trans. Magn.* **36** 3068–70
- [206] Lima C S and Baibich M N 2016 Influence of sample width on the magnetoresistance and planar Hall effect of Co/Cu multilayers *J. Appl. Phys.* **119** 33902
- [207] Chang Y C, Chang C C, Chang I, Wu J C, Wei Z-H, Lai M-F and Chang C-R 2006 Investigation of permalloy cross structure using magnetic force microscope and magnetoresistance measurement *J. Appl. Phys.* **99** 08B710
- [208] Fermon C and Pannetier-Lecoœur M 2013 Noise in GMR and TMR sensors *Giant Magnetoresistance (GMR) Sensors* (Berlin: Springer) pp 47–70
- [209] Dalslet B T, Damsgaard C D, Donolato M, Strømme M, Strømberg M, Svedlindh P and Hansen M F 2011 Bead magnetorelaxometry with an on-chip magnetoresistive sensor *Lab Chip* **11** 296–302
- [210] Jen S U, Wang P J, Tseng Y C and Chiang H P 2009 Planar Hall effect of permalloy films on Si(111), Si(100), and glass substrates *J. Appl. Phys.* **105** 07E903
- [211] Oh S J, Le T T, Kumar S A, Kim G W, Rao B P and Kim C 2007 Etching effect on exchange anisotropy in NiFe/Cu/NiFe/IrMn spin-valve structure for an array of PHR sensor element 2007 2nd IEEE Int. Conf. on Nano/Micro Engineered and Molecular Systems pp 1183–5
- [212] Hung T Q, Quang P H, Thanh N T, Sunjong O, Bajaj B and CheolGi K 2007 The contribution of the exchange biased field direction in multilayer thin films to planar Hall resistance *Phys. Status Solidi* **244** 4431–4
- [213] Thanh N T, Chun M G, Schmalhorst J, Reiss G, Kim K Y and Kim C G 2006 Magnetizing angle dependence of planar Hall resistance in spin-valve structure *J. Magn. Mater.* **304** e84–7
- [214] Rizzi G, Lundtoft N C, Østerberg F W and Hansen M F 2012 Reversible and irreversible temperature-induced changes in exchange-biased planar hall effect bridge (pheb) magnetic field sensors *Sens. Trans.* **15** 22–34
- [215] Wesenberg D, Hojem A, Bennet R K and Zink B L 2018 Relation of planar Hall and planar Nernst effects in thin film permalloy *J. Phys. D: Appl. Phys.* **51** 244005
- [216] Lu Z Q, Pan G, Li J and Lai W Y 2001 Planar Hall effect and magnetoresistance in spin valve multilayers *J. Appl. Phys.* **89** 7215–7
- [217] Tamaha C R, Mulvaney S P, Rife J C and Whitman L J 2008 Magnetic labeling, detection, and system integration *Biosens. Bioelectron.* **24** 1–13
- [218] Wang S X and Li G 2008 Advances in giant magnetoresistance biosensors with magnetic nanoparticle tags: review and outlook *IEEE Trans. Magn.* **44** 1687–702
- [219] Baselt D R, Lee G U, Natesan M, Metzger S W, Sheehan P E and Colton R J 1998 A biosensor based on magnetoresistance technology. This paper was awarded the biosensors & bioelectronics award for the most original contribution to the congress. *Biosens. Bioelectron.* **13** 731–9
- [220] Graham D L, Ferreira H, Bernardo J, Freitas P P and Cabral J M S 2002 Single magnetic microsphere placement and detection on-chip using current line designs with integrated spin valve sensors: biotechnological applications *J. Appl. Phys.* **91** 7786–8
- [221] Schotter J, Kamp P B, Becker A, Pühler A, Reiss G and Brückl H 2004 Comparison of a prototype magnetoresistive biosensor to standard fluorescent DNA detection *Biosens. Bioelectron.* **19** 1149–56
- [222] Dalslet B T, Donolato M and Hansen M F 2012 Planar Hall effect sensor with magnetostatic compensation layer *Sens. Actuators A* **174** 1–8
- [223] Rizzi G, Westergaard Østerberg F, Dufva M and Fougat Hansen M 2014 Magnetoresistive sensor for real-time single nucleotide polymorphism genotyping *Biosens. Bioelectron.* **52** 445–51
- [224] Rizzi G, Østerberg F W, Henriksen A D, Dufva M and Hansen M F 2015 On-chip magnetic bead-based DNA melting curve analysis using a magnetoresistive sensor *J. Magn. Mater.* **380** 215–20
- [225] Rizzi G, Dufva M and Hansen M F 2017 Two-dimensional salt and temperature DNA denaturation analysis using a magnetoresistive sensor *Lab Chip* **17** 2256–63
- [226] Østerberg F W, Rizzi G, Donolato M, Bejhed R S, Mezger A, Strømberg M, Nilsson M, Strømme M, Svedlindh P and Hansen M F 2014 On-chip detection of rolling circle amplified DNA molecules from bacillus globigii spores and vibrio cholerae *Small* **10** 2877–82
- [227] Rizzi G, Dufva M and Hansen M F 2017 Magnetoresistive sensors for measurements of DNA hybridization kinetics—effect of TINA modifications *Sci. Rep.* **7** 41940
- [228] Oh S, Baek N S, Jung S D, Chung M A, Hung T Q, Anandakumar S, Rani V S, Jeong J R and Kim C 2011 Selective binding and detection of magnetic labels using PHR sensor via photoresist micro-wells *J. Nanosci. Nanotechnol.* **11** 4452–6

- [229] Bui D T, Tran M D, Nguyen H D and Nguyen H B 2013 High-sensitivity planar Hall sensor based on simple giant magneto resistance NiFe/Cu/NiFe structure for biochip application *Adv. Nat. Sci. Nanosci. Nanotechnol.* **4** 15017
- [230] Sinha B, Ramulu T S, Kim K W, Venu R, Lee J J and Kim C G 2014 Planar Hall magnetoresistive aptasensor for thrombin detection *Biosens. Bioelectron.* **59** 140–4
- [231] Kim S, Torati S R, Talantsev A, Jeon C, Lee S and Kim C 2020 Performance validation of a planar Hall resistance biosensor through beta-amyloid biomarker *Sensors* **20** 434
- [232] Bajaj B, Thanh N T and Kim C G 2007 Planar Hall effect in spin valve structure for DNA detection immobilized with single magnetic bead 2007 7th IEEE Conf. on Nanotechnology (IEEE NANO) pp 1033–6
- [233] Østerberg F W, Rizzi G and Hansen M F 2013 On-chip measurements of brownian relaxation of magnetic beads with diameters from 10 nm to 250 nm *J. Appl. Phys.* **113** 154507
- [234] Volmer M and Avram M 2012 Microbeads detection using spin-valve planar hall effect sensors *J. Nanosci. Nanotechnol.* **12** 7456–9
- [235] Sinha B, Anandakumar S, Oh S and Kim C 2012 Micro-magnetometry for susceptibility measurement of superparamagnetic single bead *Sens. Actuators A* **182** 34–40
- [236] Kim K W, Reddy V, Torati S R, Hu X H, Sandhu A and Kim C G 2015 On-chip magnetometer for characterization of superparamagnetic nanoparticles *Lab Chip* **15** 696–703
- [237] Kamara S, Tran Q H, Davesne V, Félix G, Salmon L, Kim K, Kim C G, Bousseksou A and Terki F 2017 Magnetic susceptibility study of sub-pico-emu sample using a micromagnetometer: an investigation through bistable spin-crossover materials *Adv. Mater.* **29** 1–5
- [238] Hung T Q *et al* 2013 Room temperature magnetic detection of spin switching in nanosized spin-crossover materials *Angew. Chem., Int. Ed.* **52** 1185–8
- [239] Chui K M, Adeyeye A O and Li M-H 2007 Detection of a single magnetic dot using a planar Hall sensor *J. Magn. Mater.* **310** e992–3
- [240] Volmer M, Avram M and Avram A M 2015 Simulation and experimental results on manipulation and detection of magnetic nanoparticles using planar hall effect sensors 2015 Int. Semiconductor Conf. (CAS) pp 117–20
- [241] Kim K W, Torati S R, Reddy V and Yoon S S 2014 Planar hall resistance sensor for monitoring current *J. Magn.* **19** 151–4
- [242] Persson A, Bejhed R S, Østerberg F W, Gunnarsson K, Nguyen H, Rizzi G, Hansen M F and Svedlindh P 2013 Modelling and design of planar Hall effect bridge sensors for low-frequency applications *Sens. Actuators A* **189** 459–65
- [243] Persson A, Bejhed R, Gunnarsson K, Nguyen H, Dalslet B T, Oesterberg F W, Hansen M F and Svedlindh P 2011 Low-frequency picotesla field detection with planar Hall effect bridge sensors *Mater. Sci.* 1–17 ([www.diva-portal.org/smash/record.jsf?pid=diva2%3A416049&dsid=2652](http://www.diva-portal.org/smash/record.jsf?pid=diva2%3A416049&dsid=2652))
- [244] Volmer M and Neamtu J 2008 Micromagnetic characterization of a rotation sensor based on the planar Hall effect *Phys. B* **403** 350–3
- [245] Dalslet B T, Damsgaard C D, Freitasy S C, Freitas P P and Hansen M F 2008 Bead capture and release on a magnetic sensor in a microfluidic system *SENSORS, 2008 IEEE* pp 242–5
- [246] Osterberg F W, Dalslet B T, Damsgaard C D, Freitas S C, Freitas P P and Hansen M F 2009 Bead capture on magnetic sensors in a microfluidic system *IEEE Sens. J.* **9** 682–8
- [247] Østerberg F W, Rizzi G, De La Torre T Z G, Strömberg M, Strømme M, Svedlindh P and Hansen M F 2013 Measurements of Brownian relaxation of magnetic nanobeads using planar Hall effect bridge sensors *Biosens. Bioelectron.* **40** 147–52
- [248] Osterberg F W, Dalslet B T, Snakenborg D, Johansson C and Hansen M F 2010 Chip-based measurements of brownian relaxation of magnetic beads using a planar Hall effect magnetic field sensor *AIP Conf. Proc.* **1311** 176–83
- [249] Hansen T B G, Damsgaard C D, Dalslet B T and Hansen M F 2010 Theoretical study of in-plane response of magnetic field sensor to magnetic beads magnetized by the sensor self-field *J. Appl. Phys.* **107** 124511
- [250] Damsgaard C D and Hansen M F 2008 Theoretical study of in-plane response of magnetic field sensor to magnetic beads in an in-plane homogeneous field *J. Appl. Phys.* **103** 064512
- [251] Anon Magnetic diagnostic assay for neurodegenerative diseases MADIA Project H2020 CORDIS (European Commission)
- [252] An B W, Shin J H, Kim S-Y, Kim J, Ji S, Park J, Lee Y, Jang J, Park Y-G and Cho E 2017 Smart sensor systems for wearable electronic devices *Polymers* **9** 303
- [253] Dahiya A S *et al* 2020 Review—energy autonomous wearable sensors for smart healthcare: a review *J. Electrochem. Soc.* **167** 37516
- [254] Lim H-R, Kim H S, Qazi R, Kwon Y-T, Jeong J-W and Yeo W-H 2020 Wearable flexible hybrid electronics: advanced soft materials, sensor integrations, and applications of wearable flexible hybrid electronics in healthcare, energy, and environment *Adv. Mater.* **32** 2070116
- [255] Lee S, Yoon J, Lee D, Seong D, Lee S, Jang M, Choi J, Yu K J, Kim J and Lee S 2020 Wireless epidermal electromyogram sensing system *Electronics* **9** 269
- [256] Kim K, Kim B and Lee C H 2020 Printing flexible and hybrid electronics for human skin and eye-interfaced health monitoring systems *Adv. Mater.* **32** 1902051
- [257] Melzer M, Makarov D and Schmidt O G 2019 A review on stretchable magnetic field sensorics *J. Phys. D: Appl. Phys.* **53** 83002
- [258] Jeong W, Kim M, Ha J-H, Binti Zulkifli N A, Hong J-I, Kim C and Lee S 2019 Accurate, hysteresis-free temperature sensor for health monitoring using a magnetic sensor and pristine polymer *RSC Adv.* **9** 7885–9
- [259] Kim S, Oh S, Kim K B, Jung Y, Lim H and Cho K 2018 Design of a bioinspired robotic hand: magnetic synapse sensor integration for a robust remote tactile sensing *IEEE Robot. Autom. Lett.* **3** 3545–52